Attenuation models (Q_P and Q_S) in three dimensions of the southern California crust: Inferred fluid saturation at seismogenic depths

Egill Hauksson[1] and Peter M. Shearer[2]

Received 19 July 2005; revised 17 January 2006; accepted 30 January 2006; published 2 May 2006.

[1] We analyze high dynamic range waveform spectra to determine t^* values for both P and S waves from earthquakes in southern California. We invert the t^* values for three-dimensional (3-D) frequency-independent Q_P and Q_S regional models of the crust. The models have 15 km horizontal grid spacing and an average vertical grid spacing of 4 km, down to 22 km depth, and extend from the U.S.-Mexico border to the Coast Ranges in the south and Sierra Nevada in the north. In general, Q_P and Q_S increase rapidly with depth, consistent with crustal densities and velocities. The 3-D Q_P and Q_S models image the major tectonic structures and to a much lesser extent the thermal structure of the southern California crust. The near-surface low Q_P and Q_S zones coincide with major sedimentary basins such as the San Bernardino, Chino, San Gabriel Valley, Los Angeles, Ventura, and Santa Maria basins and the Salton Trough. In contrast, at shallow depths beneath the Peninsular Ranges, southern Mojave Desert, and southern Sierras, we image high Q_P and Q_S zones, which correspond to the dense and high-velocity rocks of the mountain ranges. Several clear transition zones of rapidly varying Q_P and Q_S coincide with major late Quaternary faults and connect regions of high and low Q_P and Q_S. At midcrustal depths, the Q_P and Q_S exhibit modest variation in slightly higher and lower Q_P or Q_S zones, which is consistent with reported crustal reflectivity. In general, for the southern California crust, Q_S/Q_P is greater than 1.0, suggesting partially fluid-saturated crust. A few limited regions of Q_S/Q_P less than 1.0 correspond to areas mostly outside the major sedimentary basins, including areas around the San Jacinto fault, suggesting a larger reduction in the shear modulus compared to the bulk modulus or almost complete fluid saturation.

Citation: Hauksson, E., and P. M. Shearer (2006), Attenuation models (Q_P and Q_S) in three dimensions of the southern California crust: Inferred fluid saturation at seismogenic depths, *J. Geophys. Res.*, *111*, B05302, doi:10.1029/2005JB003947.

1. Introduction

[2] The Q_P and Q_S structure or attenuation of seismic waves (Q^{-1}) varies spatially across southern California. If Q_P and Q_S are relatively low, the seismic waves are being attenuated, but if they are high, the waves travel almost undisturbed through the region. Particularly in areas where Q_P and Q_S are low, several competing effects such as intrinsic attenuation or scattering may affect the amplitude of the waves. We use a tomographic approach to invert t^* values for the three-dimensional (3-D) spatial patterns of frequency-independent Q_P and Q_S. These Q_P and Q_S patterns complement existing images of the 3-D velocity structure and mostly reflect local geology and image tectonic features such as sedimentary basins and mountain ranges (Figure 1). Regional variations in Q_P and Q_S may be caused by local impedance contrasts, chemical composition, crack structure, grain boundary movement, crustal fluids, and, to a lesser extent, temperature variations within the brittle seismogenic crust.

[3] It is common practice in most earthquake hazards calculations to determine the attenuation of ground motion using uniform Q models. As an example of the use of 3-D models, in a recent study by [*Eberhart-Phillips and McVerry*, 2003], 3-D Q_P and Q_S models were applied to determine response spectra in the New Zealand subduction environment. The 3-D models made it possible to account for the difference in attenuation through the hot mantle wedge as compared to the cold slab. The 3-D Q_P and Q_S models determined in this study can similarly be used in earthquake hazards calculations, although an appropriate calibration will be needed. In particular, trade-offs between parameters in 3-D models may exist; for instance, the frequency content of the waves used here and assumed geometrical spreading factors may differ from past studies [*Frankel et al.*, 1990; *Petukhin et al.*, 2003]. Comparison with results from forward waveform modeling also should be done with care because most waveform modeling is done at lower frequencies than used in our study [e.g., *Olsen et al.*, 2003]. However, our results do provide a guide for selecting earthquakes with representative paths for deter-

[1]Seismological Laboratory, California Institute of Technology, Pasadena, California, USA.
[2]Institute of Geophysics and Planetary Physics, Scripps Institution of Oceanography, University of California, San Diego, La Jolla, California, USA.

0148-0227/06/2005JB003947$09.00

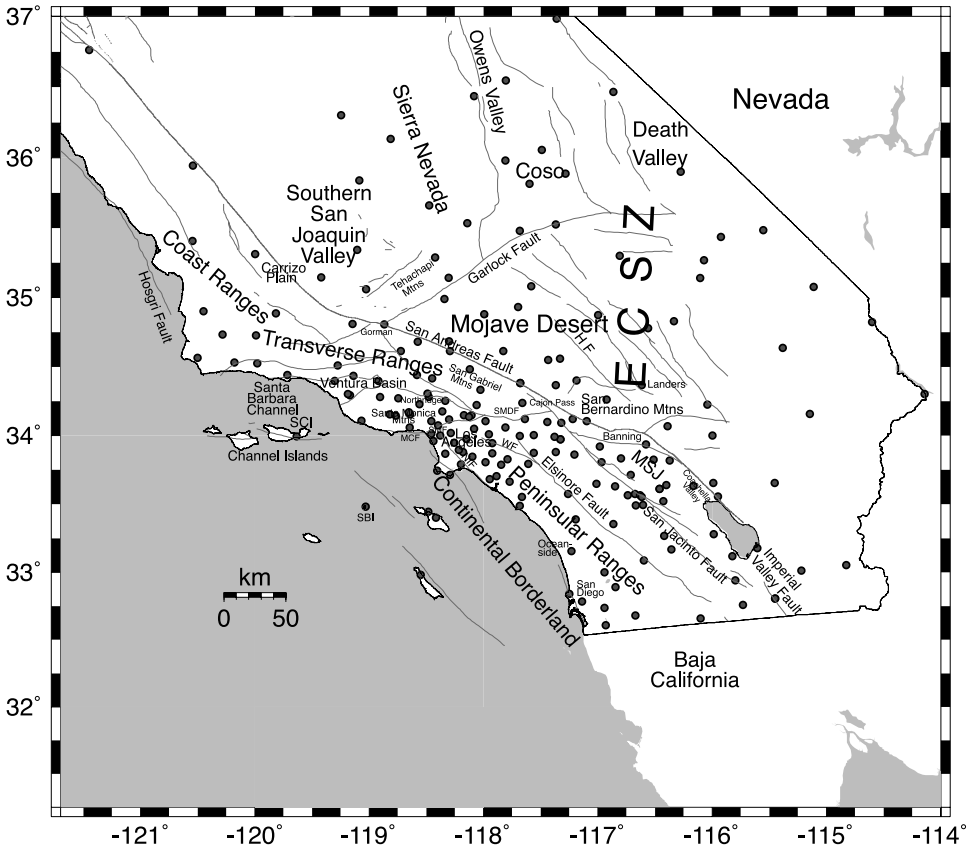

Figure 1. Map showing geographical features in the study area and seismic stations that recorded the data (solid circles). Major late Quaternary faults are also shown [*Jennings*, 1994]. ECSZ, Eastern California Shear Zone; HF, Hellendale fault; MCF, Malibu Coastal fault; MSJ, Mount San Jacinto; NIF, Newport-Inglewood fault; WF, Whittier Fault; SBI, Santa Barbara Island; SCI, Santa Cruz Island.

mining an average attenuation relationship for an engineering study.

1.1. Previous Q Studies Using Data From Southern California

[4] Most past Q studies in southern California have focused on specific data sets as well as particular issues, such as the size of near-surface Q, possible frequency dependence or the relative role of scattering versus intrinsic attenuation. Several studies have shown that Q is low in the near surface, in particular in sedimentary basins [e.g., *Hauksson et al.*, 1987; *Aster and Shearer*, 1991; *Abercrombie*, 1997]. In a detailed study of seismograms from the Cajon Pass borehole in southern California, *Adams and Abercrombie* [1998] showed that attenuation in the near surface is frequency-dependent. In a more regional study, *Raoof et al.* [1999] used regression analysis and waveform data from 17 TERRAscope stations in southern California to relate the logarithm of measured ground motion to excitation, site, and propagation effects. They showed that the frequency dependence of Q is $Q(f) = 180\, f^{0.45}$ for the frequency range 0.25 to 5.0 Hz. In contrast, *Frankel et al.* [1990] using 3–30 Hz data determined an average Q_S of 800 for southern California and inferred that Q_S could be considered frequency-independent if a strong geometrical spreading factor ($R^{-1.9}$) was assumed. The relative contribution of scattering and intrinsic attenuation can vary significantly in a region like southern California as *Frankel* [1991] showed. He inferred that intrinsic attenuation is greater than scattering attenuation in the frequency range 1 to 20 Hz.

[5] Using a similar approach as applied in our study, *Schlotterbeck and Abers* [2001] analyzed data from the early days of broadband stations, operated by the Southern California Seismic Network (SCSN/TriNet), to show that significant spatial variations in Q_P and Q_S exist beneath southern California. They interpreted these variations in Q as a heterogeneous distribution of crustal temperatures, with notably high temperatures beneath the Imperial Valley and anomalously elevated crustal temperatures beneath the San Gabriel Mountains. Previously, *Ho-Liu et al.* [1988] applied 3-D attenuation tomography to identify low Q bodies at depth beneath the Imperial Valley and Coso-Indian Wells region. Our study extends these and other previous studies by using a 3-D velocity model and by analyzing a much larger data volume than was available before.

1.2. Goals of This Study

[6] We have determined t^* values from high-frequency P and S waves traveling through the southern California crust. We have inverted these t^* values for 3-D Q_P and Q_S tomographic models. We compare these models with the regional tectonics as well as the 3-D velocity models of *Hauksson* [2000] to facilitate understanding of the origin of

the 3-D variations in Q_P and Q_S. In addition, we compare the 3-D Q_P and Q_S models themselves and determine the 3-D Q_S/Q_P patterns across the region. In particular, the Q_S/Q_P may reveal the types of attenuation mechanisms and possible effects of crustal fluids on attenuation.

[7] The 3-D Q_P and Q_S models of the southern California crust image many diverse geologic and tectonic features. We are interested in finding out how well the near-surface patterns of attenuation match the local geology to understand the implications of these models for seismic hazards. Similarly, at midcrustal depths, we are looking for anomalous structures that may not have been mapped previously. For instance, we seek to identify the spatial extent of low or high Q zones or if anomalous regions of high or low Q exist at depth that can be associated with past tectonic history or zones of anomalous temperatures. The brittle-ductile transition could spatially coincide with changes in the material composition or temperature, which may be imaged as sudden changes in Q with depth [*Petukhin et al.*, 2003]. Similarly, we are interested in understanding if attenuation losses are significantly different in the reflective lower crust as compared to the upper crust.

2. Data and Methods

2.1. Determining t^*

[8] We analyze seismograms from earthquakes that were recorded by the SCSN across southern California (Figure 2). We follow the approach of *Eberhart-Phillips and Chadwick* [2002], as initially developed by *Rietbrock* [2001] and *Scherbaum* [1990], to determine velocity spectra and to invert for t^* values.

[9] Assuming an f^2 source model [*Brune*, 1970] and that the whole path attenuation is described by

$$t^* = t^*_{ij} + t^*_{\text{station}} \tag{1}$$

where t^*_{ij} is the whole path attenuation and t^*_{station} describes the local site effect. We use the following expression from *Eberhart-Phillips and Chadwick* [2002] for the velocity amplitude spectra:

$$A_{ij}(f) = 2\pi f \Omega_0 \frac{f_c^2}{\left(f_c^2 + f^2\right)} \exp\left[-\pi f \left(t^*_{ij} + t^*_{\text{station}}\right)\right] \tag{2}$$

[10] For each earthquake, both Ω_0 and f_c are determined along with t^*. The Ω_0 term includes geometrical spreading. Sometimes this t^* parameter is referred to as the "kappa" (k) parameter in strong motion seismology [i.e., *Anderson and Hough*, 1984; *Rietbrock*, 2001]. Numerical tests and observations have also shown that the f^2 model and frequency-independent Q provide good fits to recorded amplitude spectra [*Rietbrock*, 2001; *Shearer et al.*, 2006].

[11] To determine t^*_{ij} for each ray path, we apply the iterative approach of *Eberhart-Phillips and Chadwick* [2002]. First we invert for Ω_o, and the corner frequency, f_c using all available amplitude spectra for each event. Similar to *Eberhart-Phillips and Chadwick* [2002], we find that the Ω_0 values give reasonable scaling values when they are corrected for instrument response, although they have not been corrected for the radiation pattern, which is needed to obtain accurate seismic moment. The f_c values from this study decrease with moment but exhibit a strong scatter as observed in many previous studies of source parameters for small earthquakes [e.g., *Hough et al.*, 1991; *Lees and Lindley*, 1994; *Eberhart-Phillips and Chadwick*, 2002]. The f_c values for P spectra are about 1.7 times larger than the corner frequencies for S spectra, which was explained by *Savage* [1974] as being related to rupture processes. Applying similar methods as here, *Sarker and Abers* [1999] showed in a different study that trade-offs between t^* and f_c, source-depth effects and effects of window length on t^* were well within 1 sigma standard error, and never exceeded 10%.

[12] We have applied the techniques from *Eberhart-Phillips and Chadwick* [2002] to determine t^* for more than 5000 events (1997 to 2004) of M from 2.3 to 5.8 and have obtained successful t^* measurements for a total of ~340,000 seismograms. To determine the velocity spectra values from P waves, we used the high dynamic range HHZ component waveforms that are recorded by the 171 broadband stations (Figure 1). We did not include EHZ component waveforms because these are short period and have a much more limited dynamic range. For determining t^* values from S waves, we used the HHE and HHN component waveforms separately. Sample waveforms from three stations with vertical, north, and east components, and spectra with the appropriate fitting parameters are shown in Figure 3. The amplitude spectra were calculated for a 2.56 s time window around each of the P or S arrival times. A corresponding noise spectrum was also calculated for a preevent segment of data. To obtain smooth spectra, we applied a multitaper algorithm with a 2.56π-prolate taper sequence, which is equivalent to a frequency averaging of 4 Hz [*Park et al.*, 1987].

[13] To ensure the highest quality of t^* values for the inversion for Q models, we applied the following selection criteria. The P wave amplitude spectrum must be 2.0 times larger than the spectrum of the background noise in a 10 Hz wide frequency band from 2 to 30 Hz. Each event needed to have more than five t^* values to be included in the data set. The S wave spectra were selected using a lower noise threshold of 1.5 because the goal was to obtain a similar number and quality of P and S measurements of t^*. The S waves were recorded on horizontal components, which minimized the potential influence of P wave coda. However, because the background microseismic noise is always somewhat higher on horizontal components than vertical components, the low value of signal to noise is required to obtain a similar number of measurements. We assign quality values of 0, 1, 2, 3, or 4 (where 0 is best and 4 is worst and not included in the inversion) to the t^* values as described by *Eberhart-Phillips and Chadwick* [2002]. These weights reflect how well the spectra are fit during the iterative procedure and provide one more data selection filter in addition to the signal-to-noise ratio criteria. We also excluded very small t^* values that corresponded to unrealistically large Q (larger than 3000). This criteria excluded about 10% of the t* values for P spectra and 7% of the t* for S spectra. Q models calculated with and without applying this data selection criteria are very similar because nearly all

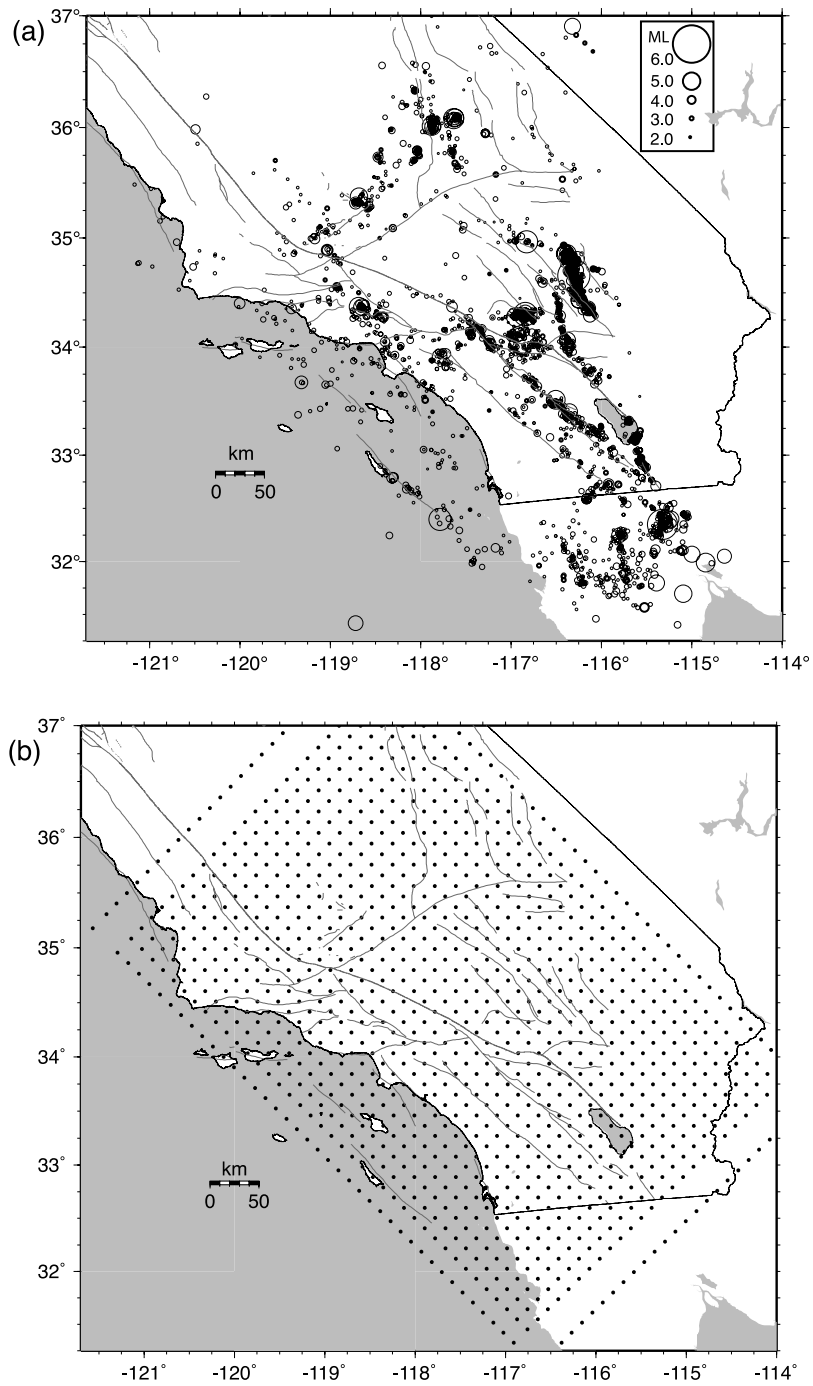

Figure 2. (a) Seismicity used to determine the Q_P and Q_S models. Size of circles is scaled by magnitude. (b) Inversion grid used to determine both Q_P and Q_S. The horizontal rectangular spacing of grid nodes is 15 km except along the edges. The depth distribution of nodes is 1.0, 4.0, 6.0, 10.0, 15.0, 17.0, 22.0, 31.0, and 33.0 km.

of the spatial variations in the 3-D Q models result from the large t^* values that correspond to Q values much less than 3000. As an independent check, we compared the t^* values determined in this study to the t^* values for the same events as analyzed by *Schlotterbeck and Abers* [2001] and found that the t^* values are very similar.

[14] As examples of the t^* values, we show the observed t^* for both P and S waves and predicted t^* from the 3-D Q_P and Q_S models from two randomly selected stations near the 1999 M7.1 Hector Mine earthquake (HEC) and near Coso (CLC) in Figure 4. The most prominent signal in the data is the increase in observed t^* values with distance, which is the signal that is being fit in the 3-D Q model inversion. The

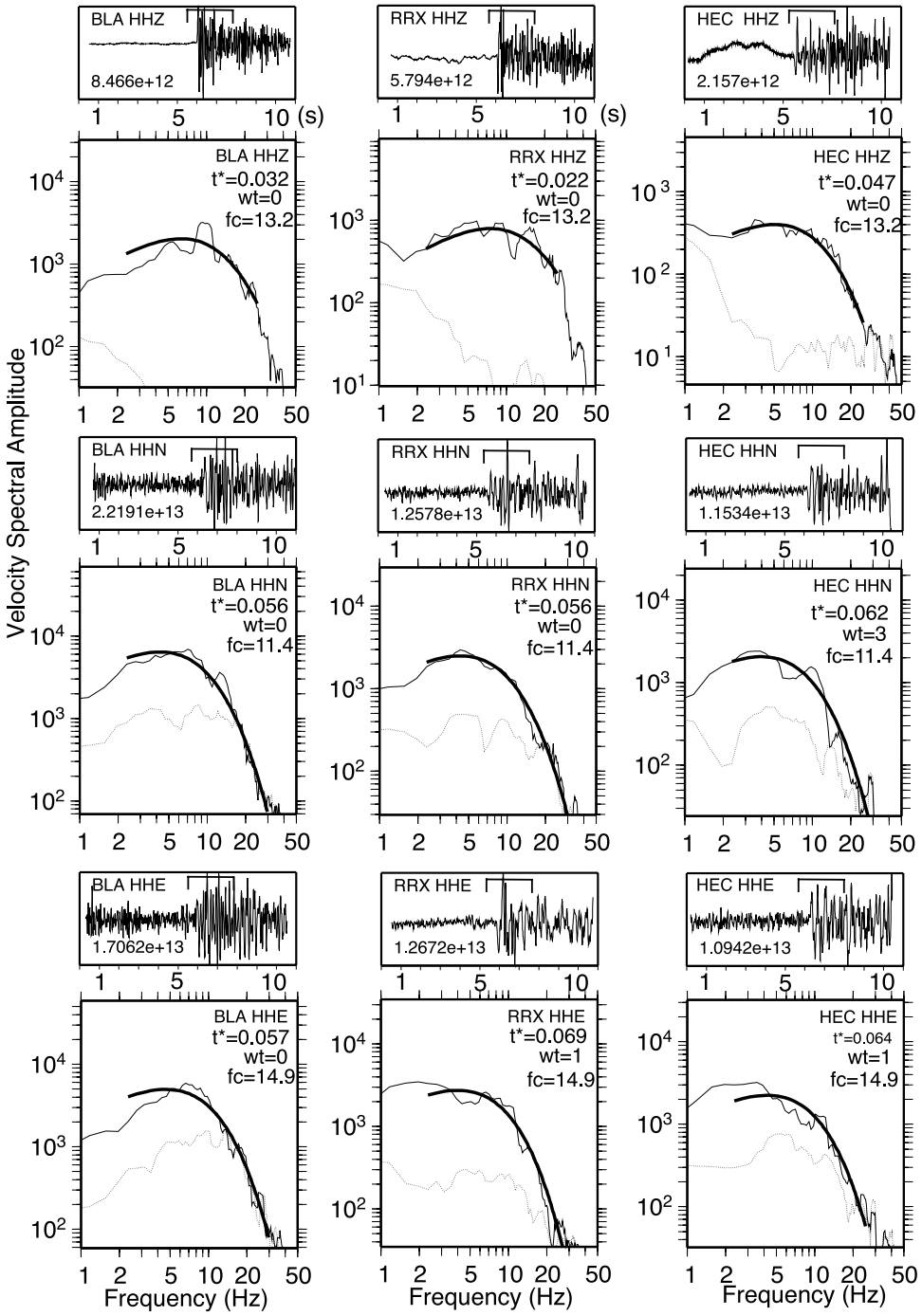

Figure 3. Sample broadband seismograms from one earthquake located near Big Bear, southern California, as well as signal and noise spectra for three SCSN stations, BLA, RRX, and HEC and vertical, north, and east components are shown. The plotted waveform window that is 10.24 s long, also includes the 2.56 s window over which we determine the spectra (indicated by bracket) and the peak amplitude in counts. Below each waveform, the signal and preevent noise spectra are plotted. The fit to the signal spectra over the range with sufficient signal-to-noise ratio is shown as a heavy line on top of the signal spectra. Below the station and component codes, we list, t^* calculated weight that is scaled from 0 to 4 (where 0 is smallest error) and the corner frequency, f_c.

distribution of the model predicted values shows that the increase in t^* with distance and significant parts of the scatter in the t^* values are being explained by the new 3-D models. The remaining scatter in the t^* values that are not explained by the 3-D model contains random signals possibly caused by path effects related to multipathing or, less likely, source effects.

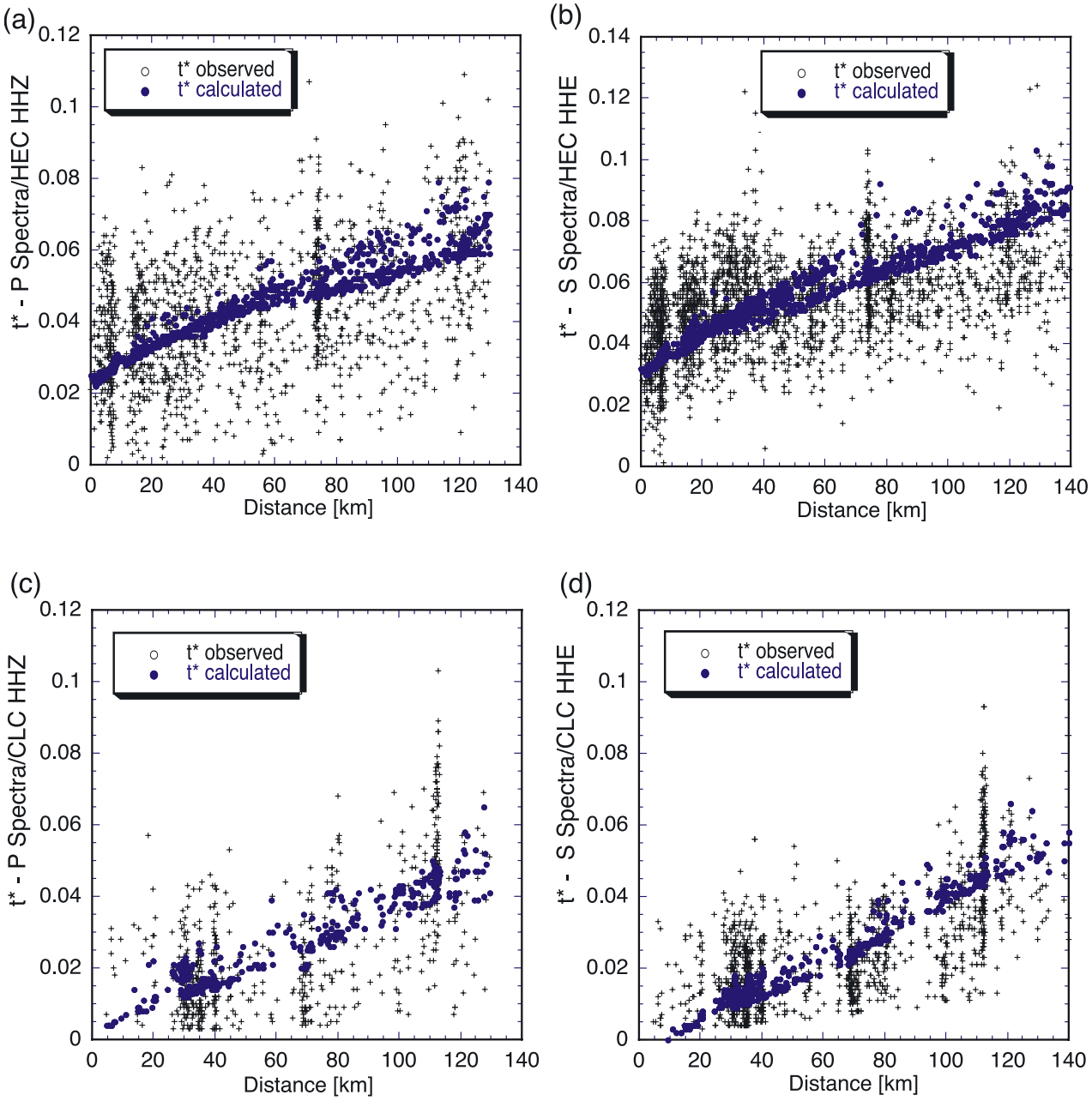

Figure 4. Observed t^* values (ttobs) and calculated t^* values (ttcal) are plotted as function of distance for both P and S spectra observed at stations HEC, Hector Mine, and CLC, China Lake, in eastern California.

2.2. Inversion for 3-D Q_P and Q_S Models

[15] The t^* values are related to both Q and the velocity structure through

$$t^* = \int_{ij} 1/\left(Q_{(x,y,z)} v_{(x,y,z)}\right) ds + t^*_{\text{station}} \qquad (3)$$

where ds is distance along the ray path from hypocenter i to station j [*Rietbrock*, 2001; *Eberhart-Phillips and Chadwick*, 2002], and $v(x, y, z)$ is the 3-D velocity model from *Hauksson* [2000].

[16] We used results from the study by *Olsen et al.* [2003], who simulated 3-D wave propagation through the Los Angeles basin, to determine the starting Q_P and Q_S models. They provided formulas $Q_S/V_S = 0.02$ (where V_S is in meters per second) and $Q_P = 1.5Q_S$ that we used to determine starting Q_P and Q_S models (Figure 5) using the 1-D V_S model from *Hauksson* [2000]. We inverted for new starting models, using the results of the previous run as a starting model. The Q_S model converged after two sets of inversions while the Q_P model converged after three sets of inversions. The 1-D Q_P models all became about 10% smaller while the 1-D Q_S models all became 10% larger than the prescribed 1-D starting model. Even if we used a

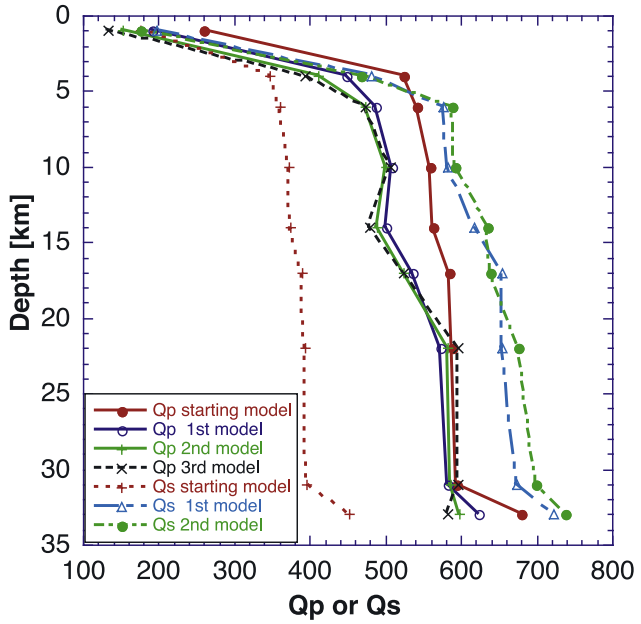

Figure 5. The 1-D Q_P and Q_S starting models, shown as a function of depth. These models were calculated using the formulas from *Olsen et al.* [2003]. Q_P models from three successive iterative inversions (Q_P first, second, and third models) and Q_S models from two successive iterative inversions (Q_S first and second models) are also shown.

starting model of $Q_S = Q_P/1.5$, the iterations toward the best 1-D starting model all ended up with a higher Q value as shown in Figure 5. Thus we had no success in matching the ratio, $Q_P/Q_S = 1.5$ as suggested by *Olsen et al.* [2003].

[17] We applied the SIMULPS2000 code by *Thurber* [1993], *Eberhart-Phillips* [1993], and *Thurber and Eberhart-Phillips* [1999] to determine Q_P and Q_S at 3-D grid nodes. Previously, SIMULPS has been applied to determine 3-D Q models in the 1989 Loma Prieta aftershock region [*Rietbrock*, 1996], the Kobe aftershock region [*Rietbrock*, 2001], the western central Andes subduction zone [*Haberland and Rietbrock*, 2001], and the shallow Hikurangi subduction zone in the Raukumara Peninsula, New Zealand [*Eberhart-Phillips and Chadwick*, 2002].

[18] We invert the t^* data for Q values on the same grid of 15 km horizontal and ~4 km vertical spacing as used by *Hauksson* [2000] (Figure 2). The approximate ray tracing was done within the *Hauksson* [2000] model. During the inversion, the hypocenters and origin times were kept fixed, which simplifies the inversion. We used the double-difference relocated hypocenters from *Hauksson and Shearer* [2005], or if these were not available, we relocated the hypocenters using the 3-D model from *Hauksson* [2000]. Only grid nodes that were illuminated with at least 20 rays are inverted.

[19] We used the derivative weighted sum (DWS) to evaluate the quality of the solution (see Appendix A). The DWS measures the ray density in the neighborhood of every node. In figures, the model areas that have small DWS values (less than 1000) are not shown. Numerous past studies have shown that the DWS values track fairly well the diagonal elements of the resolution matrix and possible smearing as indicated by the spread function. For instance, *Rietbrock* [2001] used the spread function, as defined by *Michelini and McEvilly* [1991], to determine smearing within his Q_P model of the Kobe region and show good agreement with the DWS values. Similarly, *Hauksson* [2000] showed that the DWS values also follow the spread function values closely and high DWS values identify model areas of high resolution and low smearing.

[20] We inverted the t^* data for Q_P and Q_S models independently. First, for each model we inverted the t^* data using a distance cutoff at 60 km, and linear tapering from weight of 1.0 at 60 km to 0.0 at 75 km distance. Second, we used the Q model from the first set of iterations as a starting model and inverted the data again using a distance cutoff of 120 km, and tapering to a weight of 0.0 at 140 km distance. This choice of distance cutoff parameters is consistent with the velocity model distance cutoff parameters used by *Hauksson* [2000] and *Atkinson and Mereu* [1992], who pointed out that *Lg* was prominent beyond 130 km. Similarly, *Erickson et al.* [2004] who studied attenuation of *Lg* waves in the continental United States analyzed data at distances greater than 110 km. The two step approach ensured that rapid near-surface changes in Q were first included in the model to minimize the possibility of smearing into the deeper layers. During the second step, we also inverted for station residuals using large damping.

[21] The choice of reasonable damping for the least squares inversion was made by using the approach of *Eberhart-Phillips* [1986]. We inspected trade-off curves that were calculated using different damping values, for reduction in weighted root-mean-square residual (RMS) and model length or the solution variance. The preferred value of damping was chosen to minimize the data variance with minimal increase in model length. The RMS was reduced on the average for many different inversions from 0.26 [s] to 0.16 [s] or 30%. This reduction in RMS can be compared with 3-D velocity inversions where the decrease is often two or three times as large.

3. Results

3.1. The 3-D Q_P and Q_S Models

[22] The 3-D Q_P and Q_S models exhibit significant spatial variations across southern California (Figures 6 and 7). This spatial distribution of Q_P and Q_S values images the real distribution of heterogeneities as changes in the amplitudes of Q_P and Q_S. However, the Q_P and Q_S amplitudes may be reduced or broadened depending on ray density, availability of crossing rays, and the source-receiver distribution (see Appendix A). Some reduction in amplitude and broadening of Q_P or Q_S features or smearing may occur, especially in regions along the edges of the seismic network where the ray coverage is somewhat sparse or no crossing rays are available [*Eberhart-Phillips and Chadwick*, 2002]. Outside the perimeter of the network, the model is not resolved because there are no rays passing through that part of the model. We use the ray density or the derivative weighted sum (DWS) to identify and blank out model areas with poor model resolution.

[23] The highs and lows in Q_P and Q_S vary sometimes by a factor of 10 in the top 1 km layer and correspond well to geology (Figures 6 and 7). The most striking near-surface

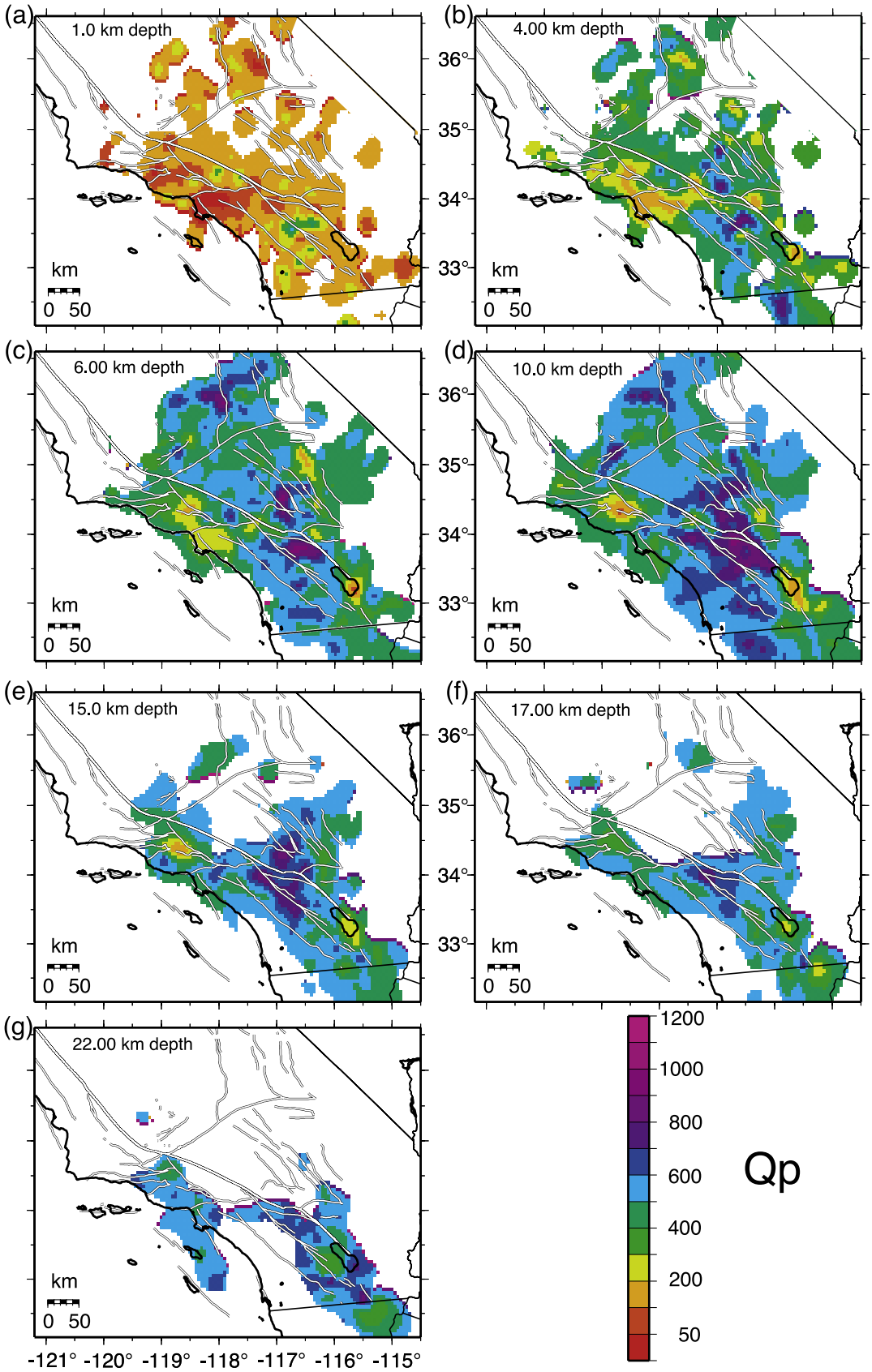

Figure 6. The 3-D Q_P model shown in map view in eight depth sections, at 1, 4, 6, 10, 15, 17, and 22 km. The color bar shows the variations in Q_P. The model is not shown in areas with sparse ray coverage or where the derivative weighted sum (DWS) is less than 2000. Major late Quaternary faults are also shown [*Jennings*, 1994].

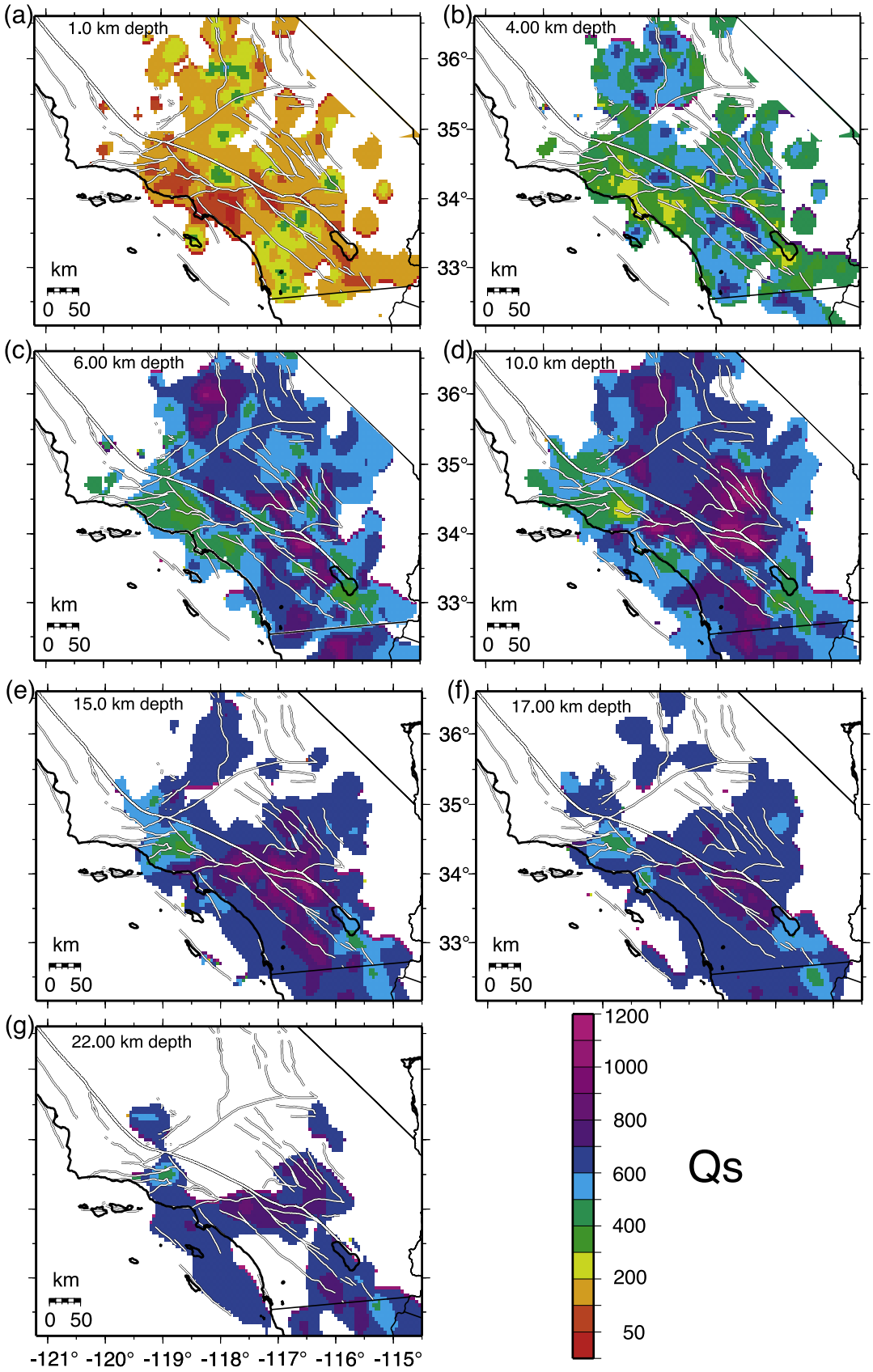

Figure 7. The 3-D Q_S model shown in map view in eight depth sections, at 1, 4, 6, 10, 15, 17, and 22 km. The color bar shows the variations in Q_S. The model is not shown in areas with sparse ray coverage or where the derivative weighted sum (DWS) less than 1000. Major late Quaternary faults are also shown [*Jennings*, 1994].

zones of low Q_P and Q_S extend from the San Bernardino Basin, across the Chino Basin, San Gabriel Valley, into the Los Angeles Basin. The low Q_P and Q_S values in the east Ventura basin are prominent from the surface down to depths of 15 km, the deepest part of the Ventura basin. This anomaly may be related to low heat flow and high pore fluid pressures in the basin sediments [*Crowell*, 1987]. The western spatial extent of the low Q_P and Q_S Ventura anomaly is in part limited by a lack of ray paths to the west. Farther to the northwest, low near-surface Q_P and Q_S are also imaged in the Santa Maria basin. Similarly, anomalous low Q_P and Q_S zones coincide with the Salton Trough where the near-surface low Q_P and Q_S are associated with the sediments and the deeper moderately reduced Q_P and average Q_S may be associated with elevated midcrustal temperatures.

[24] Some of the spatial variations in Q_P and Q_S appear to be terminated by local fault structure, where on one side of a fault the Q values may be significantly different than on the other. Such rapid changes in Q_P and Q_S values occur along the San Jacinto and Elsinore faults (Figures 6b, 6c, 7b, and 7c). Similarly, the San Andreas fault also brackets higher Q_P and Q_S values in the Peninsular Ranges and the northwestern Mojave (Figures 6c, 6d, 7c, and 7d). At depths greater than 10 km, the variations within the Q_P and Q_S models appear to be less fault controlled than at shallow depth.

[25] As expected, the mountain ranges such as Peninsular Ranges, San Bernardino Mountains, Mojave Desert, and the southern Sierras exhibit moderate Q_P and Q_S values at the surface and higher values in the depth range of 5 km to 22 km. The high Q_P and Q_S values form complex zones that differ significantly in this depth range, suggesting the presence of discrete structures with spatial scales of 10 to 50 km. For instance, the 10 km depth slice areas of high Q_P are mostly limited to the southern Mojave and the central Peninsular Ranges. In comparison, the corresponding high Q_S zone extends from the southernmost Peninsular Ranges, across the Mojave Desert, and into the southern Sierra Nevada. At greater depths, the limited high Q_P areas of the Peninsular Ranges and the south central Mojave also contrast with the extensive high Q_S zones beneath most of southern California. In detail, there are also significantly different small-scale spatial changes in Q_P and Q_S when we compare their amplitudes within the Peninsular Ranges that are cross cut by the Elsinore, San Jacinto, and San Andreas faults.

[26] We have included the 15 and 17 km deep layers in the model to image the transition of material properties from the upper into the lower crust. In general, the Q values increase with depth and the high Q_P and Q_S zones broaden out at these and greater depths, suggesting the absence of a contiguous southern California wide low Q zone at the depths below the brittle-ductile zone [*Nazareth and Hauksson*, 2004].

[27] The depth distribution of Q_P and Q_S illustrates how much larger the Q_S values are than the Q_P values (Figure 8). Both Q_P and Q_S exhibit low values in the near surface and illuminate the much higher values below depths of 4 to 6 km. In the near surface, the Ventura, Los Angeles, and San Bernardino, and several other smaller basins in the eastern Mojave Desert exhibit a clear signature of low Q values. At depth the character of the distribution of low and high Q_P and Q_S values varies significantly. The cross sections A and B coincide approximately with the LARSE seismic survey lines carried out in 1999 and 1994. Both cross sections image high Q features beneath the Santa Monica Mountains, Los Angeles basin and San Gabriel Valley, which correspond to high-velocity features identified by *Fuis et al.* [2003].

3.2. The t^* Station Residuals

[28] During the inversion we have deliberately applied strong damping to the station residuals and small damping to the model to allow the 3-D Q model to include as much of the signal as possible. As a result of this approach, near-surface geology, including the basin related signals, were mostly included in the model instead of appearing in the station residuals. There is a bigger range in the values of the $t^*(Q_S)$ station residuals than the $t^*(Q_P)$ residuals, as can be seen in map view (Figure 9). The negative residuals are more common in the high near-surface Q areas whereas the positive residuals are more common in the low near-surface Q areas. There is no simple relationship between the station residuals and elevation of the stations, in part because the near-surface geology has been included in the model.

[29] The $t^*(Q_P)$ and $t^*(Q_S)$ station residuals are correlated with a correlation coefficient of 0.6 suggesting that these residuals are partially related to the same unmodeled part of the Q and velocity structure. Such unmodeled structures may be the fine-scale structure of the impedance contrast between the batholithic terrains and the sedimentary basins or localized variations in fluid saturation of different crustal layers. In a few cases minor basins may not be included in the 15 by 15 km grid and thus appear as local station residuals. Alternatively, the station residuals could be related to multipathing along edges of basins or along major fault zones such as the San Jacinto fault.

[30] Station corrections for local magnitude (M_L) are available for 116 SCSN stations [*Kanamori et al.*, 1993]. We compared these M_L station corrections and the $t^*(Q_S)$ station residuals from both 1-D and 3-D Q_S models (Figure 10). First, we calculated the $t^*(Q_S)$ model station residuals while keeping the 1-D Q_S model fixed. Second, we calculated the 3-D model $t^*(Q_S)$ station residuals as part of the inversion for the 3-D Q_S model. The $t^*(Q_S)$ residuals and the M_L station corrections show an inverse relationship for both the 1-D and 3-D models though, as expected, the scatter is much greater for the 1-D Q_S model than for the 3-D model. The low (negative) M_L corrections correspond to high wave amplification and the high $t^*(Q_S)$ values correspond to large attenuation. As shown in Figure 10b, the 3-D Q_S model significantly reduces the scatter in the $t^*(Q_S)$ residuals and reduces the mean size of all of the residuals. The mean of the large $t^*(Q_S)$ residuals is reduced more than the mean of the smaller ones, which is consistent with how the large residuals are absorbed into the 3-D Q_S model forming near-surface low Q_S features in the model.

[31] The inverse relationship between $t^*(Q_S)$ residuals and the M_L corrections is consistent with the results of *Blakeslee and Malin* [1990]. Using borehole records, they demonstrated that at lower frequencies the early coda recorded at the surface has more low-frequency content than coda recorded at depth. The effect, which decreases with increasing frequency and disappeared at 12 Hz or so,

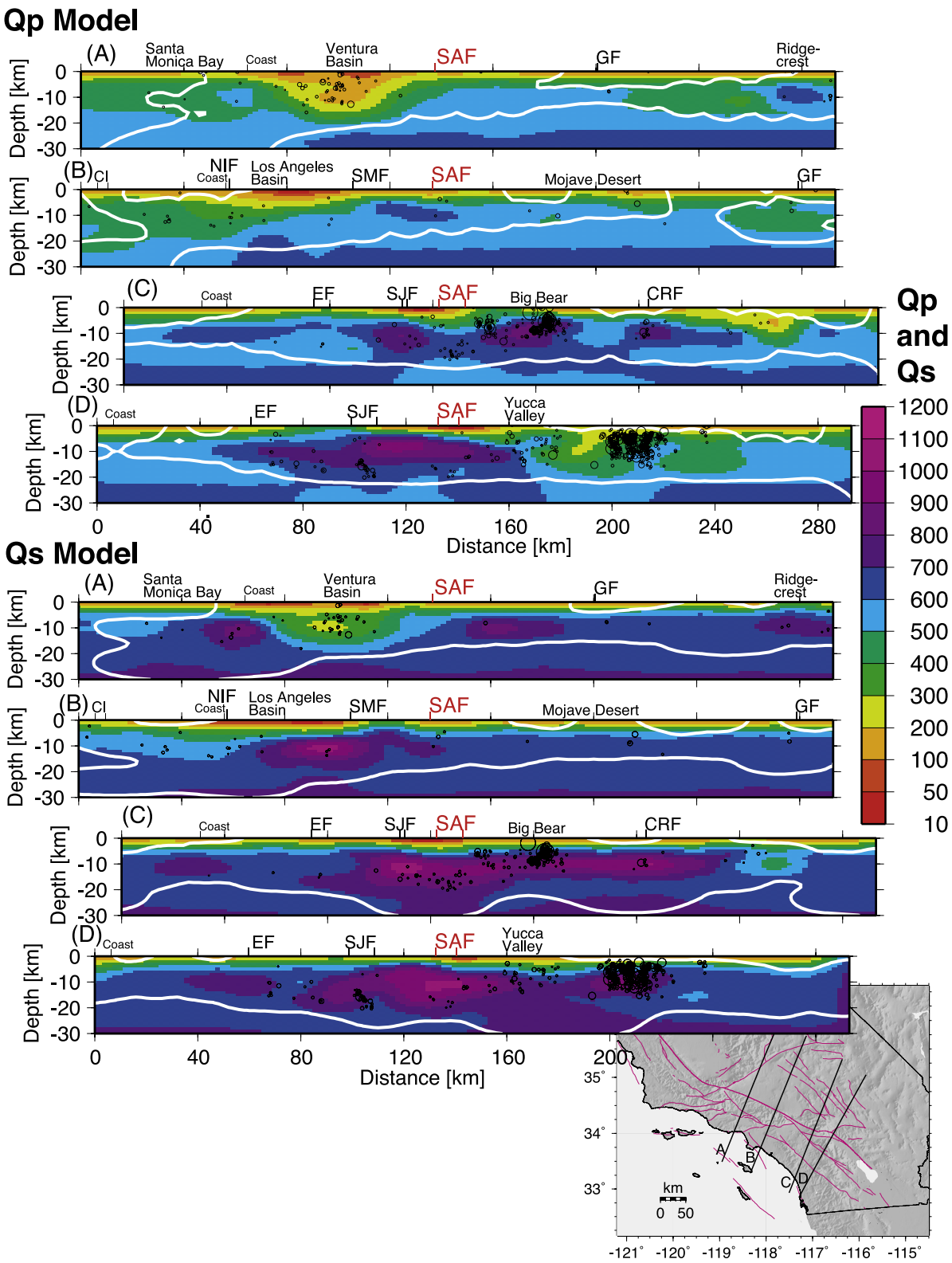

Figure 8. Cross sections through the Q_P and Q_S models extending from southwest to northeast. The map shows locations of the profiles. The white contour lines and the edges of the model outline poorly resolved areas with DWS less than 1000. CRF, Camp Rock fault; EF, Elsinore fault; GF, Garlock fault; NIF, Newport-Inglewood fault; SAF, San Andreas fault; SJF, San Jacinto fault.

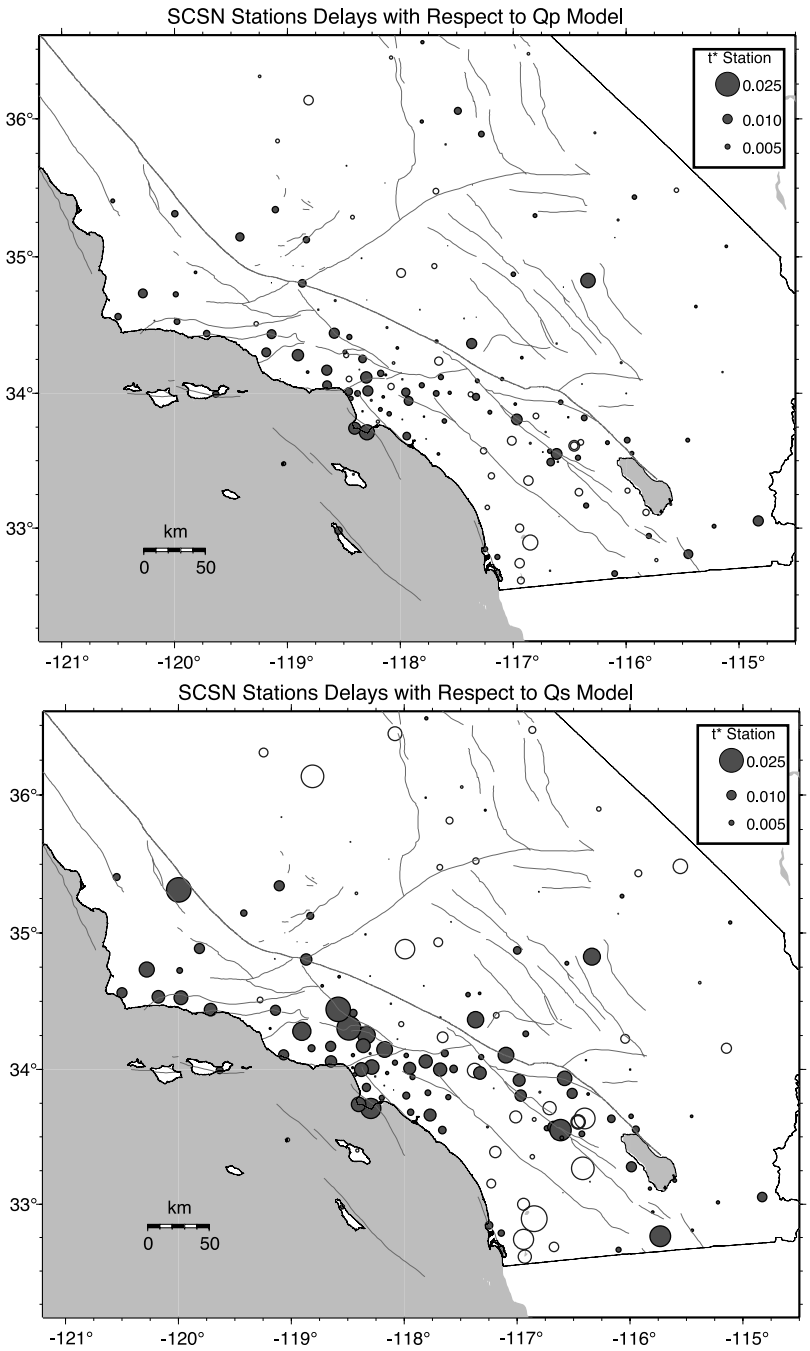

Figure 9. Maps showing t^* station residuals that correspond to the models shown in Figures 6 and 7. (top) The t^* station residuals for the Q_P model. (bottom) The t^* station residuals for the Q_S model. The solid circles indicate positive values, while the open circles indicate negative values.

can be explained as body waves converted to surface waves at the surface. Such conversion would be most effective for low Q regions or areas of large t^* residuals and would lead to larger negative M_L corrections, which is the inverse relationship presented in Figure 10.

3.3. Q_S/Q_P Ratio

[32] Theoretically, the Q_P and Q_S are related through bulk and shear attenuation, and as shown by *Knopoff* [1971], $Q_p \approx 2.25 * Q_s$ if we assume a Poissonian solid and that the bulk modulus Q_μ is very large. The Q_P and Q_S that are determined in this study are well correlated with a correlation coefficient of 0.89 and exhibit a linear fit, with Q_S being larger than Q_P on the average (Figure 11). The histogram distribution of the Q_S/Q_P values is fairly symmetric with a median of 1.2 and mean of 1.3. This observation of $Q_S/Q_P > 1.0$ which is opposite to the result of *Knopoff* [1971] can be explained, if we include the contribution of crustal pore fluids to the attenuation of seismic waves. For instance, the laboratory data analyzed by *Toksoz et al.* [1979] demonstrate that fluid–saturation plays a role in controlling Q within the seismogenic crust. They showed that Q_P was smaller than Q_S for partially

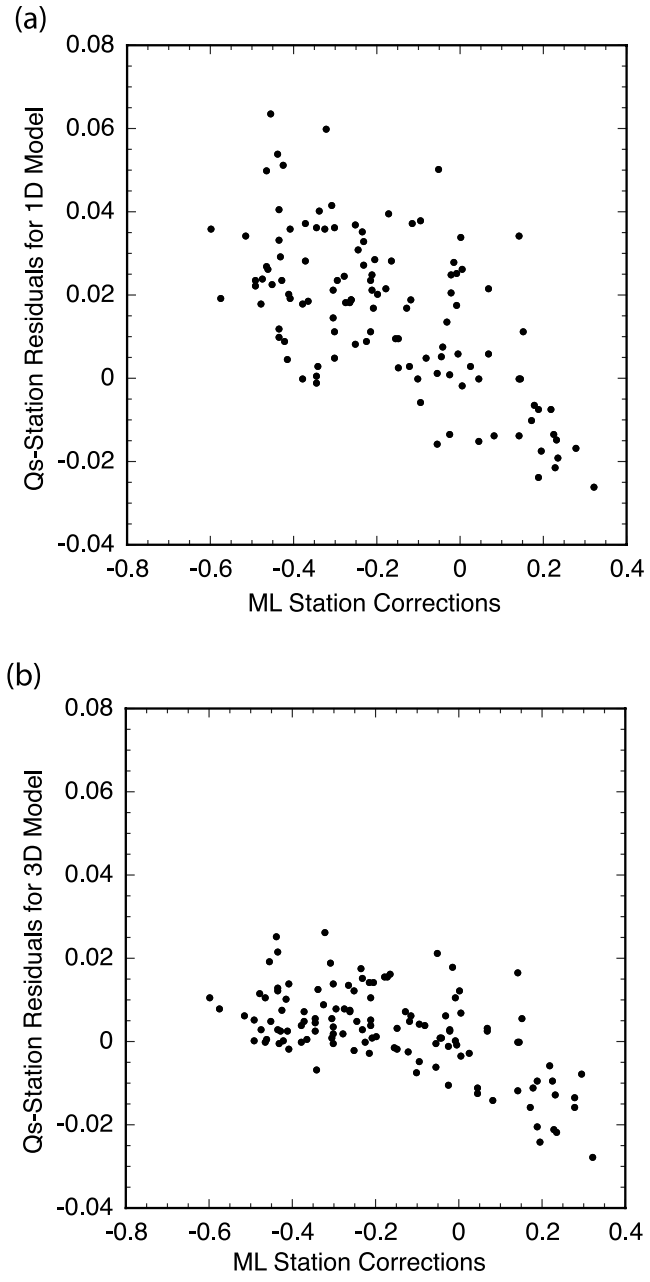

Figure 10. (a) The $t^*(Q_S)$ station residuals calculated for the 1-D Q_S model versus the M_L station corrections from *Kanamori et al.* [1993]. (b) The $t^*(Q_S)$ station residuals calculated for the 3-D Q_S model versus the same M_L station corrections.

fluid-saturated rocks, whereas Q_P was 10 to 25% larger than Q_S in fully fluid-saturated rocks at both low and high pressures, as measured at ultrasonic frequencies using pulse technique amplitudes.

[33] The detailed 3-D spatial distribution of Q_S/Q_P across most of southern California reveals that on average $Q_S/Q_P > 1$ (Figure 12). In particular, at a depth of 1 km prominent $Q_S/Q_P > 1$ zones are more common in the southern Sierra, Ridgecrest, central Mojave, and Los Angeles basin than other regions. In the depth range from 4 to 10 km, several zones of $Q_S/Q_P > 1$ are also imaged in the greater Coso region, parts of the Eastern California Shear Zone, Peninsular Ranges, Los Angeles, and selected parts of the Ventura basin. These regions of $Q_S/Q_P > 1$ may be regions where scattering is a dominant attenuation mechanism or possibly where acoustic amplification increases amplitudes in the basins, which could change the relative size of Q_P and Q_S. Alternatively, relative fluid saturation may also influence the spatial distribution of the Q_S/Q_P ratio, with only partial fluid saturation where $Q_S/Q_P > 1$.

[34] The detailed 3-D spatial distribution of Q_S/Q_P reveals only limited zones of $Q_S/Q_P < 1$ (Figure 12). The most prominent $Q_S/Q_P < 1$ zones are imaged in the 1.0 to 10.0 km depth panels and a few scattered zones of smaller amplitude appear in the 15, 17, and 22 km depth panels. The shallow zones of $Q_S/Q_P < 1$ appear to be mostly within high Q regions and in some cases they surround sedimentary basins or form zones bracketed by Late Quaternary faults such as the Elsinore and San Jacinto faults. Some of the $Q_S/Q_P < 1$ zones at depths of 10 km or greater appear to be associated with the San Jacinto fault zone, which has a very high background seismicity rate. The mechanism for $Q_S/Q_P < 1$ along the San Jacinto fault zone may be reduced shear moduli through high fluid saturation. Because there is some suggestion that low Q_S correlates well with high strain rates, viscous dissipation or frictional heating may also be important. Alternatively, the fault zone may be fully fluid saturated, and thus Q_S is decreased [*Toksoz et al.*, 1979]. A possibly anomalous zone of $Q_S/Q_P < 1$ is also imaged at 22 km depth near the south shore of the Salton Sea, which could be related to elevated crustal temperatures, and the east Ventura basin, which may be related to high fluid saturation.

4. Discussion

[35] These 3-D Q_P and Q_S models of southern California provide new information about the spatial distribution of the

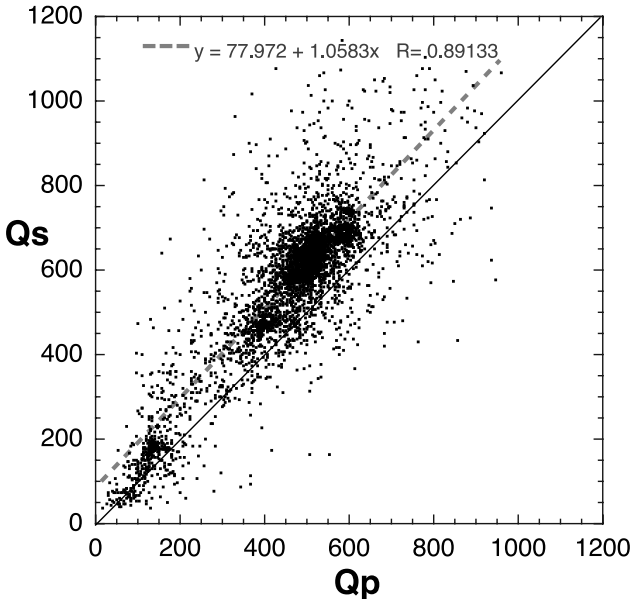

Figure 11. Q_S values plotted versus the Q_P value at the same grid node. Data from nodes with poorly resolved Q_P or Q_S values are not included. The solid line (black) has a slope of one for $Q_P = Q_S$, and the dashed line and the formula are a least squares fit to the data.

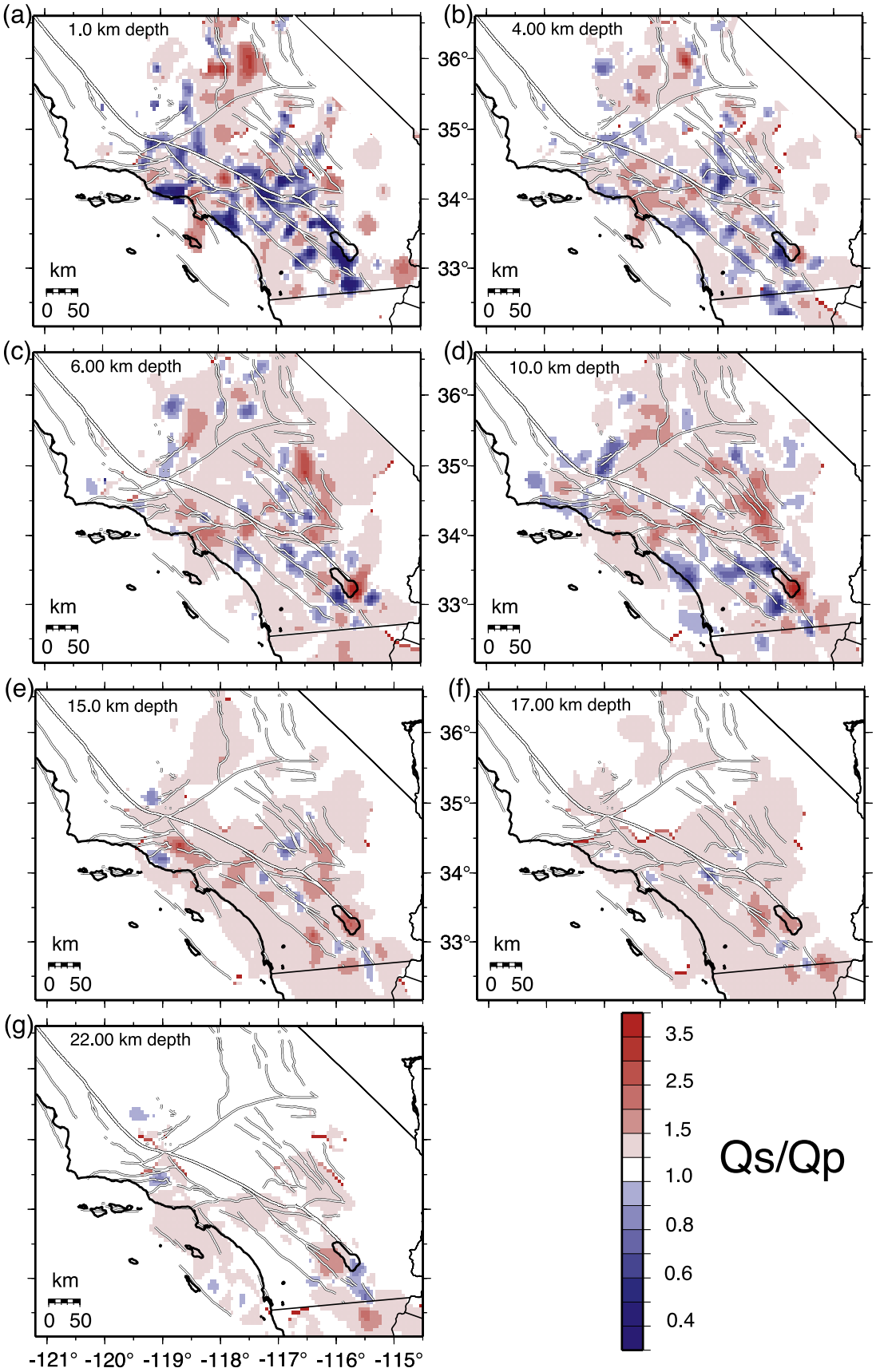

Figure 12. The 3-D Q_S/Q_P model shown in map view in eight depth sections, at 1, 4, 6, 10, 15, 17, and 22 km. The color bar shows the variations in Q_S/Q_P. The 3-D Q_S/Q_P model is only shown in regions where both Q_S and Q_P are resolved.

variation in attenuation of P and S waves. The major features of the 3-D Q_P and Q_S models are the rapid near-surface increase in Q, low Q values in sedimentary basins, high Q values within the batholiths, and alternating zones of high and low Q with depth. However, the Q_P and Q_S models do not include frequency dependence and cannot differentiate between intrinsic and scattering attenuation. Local pore fluid motion and grain boundary frictional sliding effects cause intrinsic attenuation. Scattering attenuation is caused by a redistribution of energy as it is reflected, or converted by small-scale features. Sometimes a predominance of scattering over intrinsic attenuation may cause frequency dependence, where the distribution of scatterer sizes contributes to the frequency dependence [*Frankel*, 1991].

4.1. Comparison With Other Studies Using This Method

[36] The methodology used in this study has been applied previously in regional studies elsewhere in the world. For instance, in a regional study, *Eberhart-Phillips and Chadwick* [2002] determined a Q_P model on a similar grid as used here and found values of Q_P from 30 to 880, consistent with our results. They calculated spread functions to show that within the model, the grid spacing represents the resolution of the model and the smearing is confined to the node spacing, but extends to adjacent nodes along the edges of the model. They used the 3-D Q_P, V_P, and V_P/V_S models for New Zealand to infer the presence of subducted sediments of high V_P/V_S and low Q_P at depths of 20–40 km.

[37] In a search for a specific fault zone signature, *Rietbrock* [2001] showed that low Q_P regions within the Kobe aftershock zone at shallow depth coincided with regions of high V_P/V_S and thus suggesting the presence of partially saturated cracks. His study, however, did not resolve any changes in Q_P at the depth of the main shock hypocenter. The Q_P values in the Kobe region range from 100 to 1000 or similar to what we have found in southern California. We do not have sufficient resolution in our study to resolve Q_P or Q_S anomalies associated with specific fault zones. However, there is some suggestion that $Q_S/Q_P < 1$ adjacent to the major strike-slip faults in the Peninsular Ranges, suggesting a smaller than average shear modulus.

4.2. Frequency Dependence of Q

[38] The spectral method applied in this and the studies discussed above presumes frequency-independent Q. It is thus well suited to accomplish the goal of our study, which is to provide the first-order 3-D distribution of Q but not to analyze its frequency dependence. However, if the frequency dependence of Q is spatially dependent, our 3-D models could be biased toward higher Q values in regions of positive frequency dependence.

[39] A frequently assumed form for the frequency dependence of Q in the spectral methods is $Q = Q_0 f^{\alpha}$ where α is a constant from -1.0 to 1.0. In some previous studies, similar spectral methods have been applied in California by *Lindley and Archuleta* [1992], *Lees and Lindley* [1994], *Raoof et al.* [1999], and others to evaluate the frequency dependence of Q. *Lindley and Archuleta* [1992] showed that the best fitting Q was obtained with negative values of $\alpha = -0.5$, while *Raoof et al.* [1999] found a best fit with $\alpha = 0.45$. *Lees and Lindley* [1994] tried values of α ranging from -1.0 to 0.5 and found that the tomographic inversions of data from Loma Prieta aftershocks provided very similar 3-D Q models for different values of α. Further, *Rietbrock* [2001] showed that α values ranging from 0.0 to 0.3 yielded very similar fits to the spectra determined from aftershock data of the 1995 Kobe earthquake.

[40] Other approaches that can also resolve frequency-dependent Q use time domain filtering of the waveforms and analyze how individual frequency bands decrease with distance [e.g., *Adams and Abercrombie*, 1998; *Erickson et al.*, 2004]. These techniques, like the spectral technique used here, make a variety of assumptions, which may affect how easily the frequency dependence of Q can be teased out of the data set. These studies have found positive values of α that in some cases vary with frequency, thus adding additional challenges to future inversions for frequency-dependent 3-D Q models.

[41] In general, the frequency dependence of Q is more prominent in tectonically active crust than the older shield areas of north America [*Erickson et al.*, 2004]. In particular, *Erickson et al.* [2004] studied *Lg* surface waves in the distance range of 110 to 750 km or 58 ray paths across southern California as well as in other parts of the continental United States. They were able to determine the frequency dependence of Q_{Lg} by analyzing frequency bands of data from 0.75 Hz to 12 Hz independently. Their study makes assumptions about the geometrical spreading being the same ($r^{0.5}$) over this distance range and the spectral fall off for the different sized earthquakes are presumed to be the same. Their Q_{Lg} is constant over this distance range, with Q_{Lg} of 1074 (±92) at 12 Hz, which is similar to the Q_S values obtained in this study.

[42] In a more local study, *Adams and Abercrombie* [1998] provide a comprehensive synthesis of the frequency dependence of Q from 1 Hz to 150 Hz using Cajon Pass borehole data from southern California. They showed that from 1 to 10 Hz Q is strongly frequency-dependent while above 10 Hz Q is less frequency-dependent. As an average, they found that Q_t (the sum of intrinsic and scattering Q) in the frequency range of 8–125 Hz is consistent with Q_t of 1078 (+145 or −199) similar to *Abercrombie* [1995] and the results of this study. From their results, it is reasonable to assume that Q is frequency-independent from ~10 to 20 Hz, which is the approximate middle frequency range (2 to 30 Hz) considered in this study. They also pointed out the interplay between acoustic amplification and attenuation, which is an increasing effect for waves with frequencies lower than 10 Hz. We find some evidence for such acoustic amplification when we compare our M_L station corrections with the Q_S station residuals. This evidence is exhibited as a trend of decreasing Q_S station residuals with increasing M_L corrections, which is consistent with such amplification (Figure 10).

[43] Because the methods for determining α need to be refined and determination of frequency dependence needs to be addressed in a comprehensive manner, we are only able to prove an approximate idea of how our results would be influenced by frequency-dependent Q. The frequency-independent Q values determined in this study will be larger than values determined assuming that Q is frequency-dependent. If we follow *Raoof et al.* [1999], who determined $\alpha = 0.45$ from southern California data, and assume a

frequency of 10 Hz, the corresponding Q_0 values would be ~35% of the 3-D model values determined in this study.

4.3. Comparison With Previous Southern California Studies

[44] Our results compare well to the results of *Schlotterbeck and Abers* [2001], although they used data from much fewer SCSN stations. Both studies find low Q in the Los Angeles basin and no attenuation anomalies that correspond to strike-slip zones such as the San Andreas system. Similar to the results in our study, Schlotterbeck and Abers found only a weak Q signal from the geothermal field in the Salton Trough and relatively low $Q_S/Q_P = 0.7$ to 0.5 for a limited area located near the southwest corner of the Salton Sea within the Salton Trough. They interpreted the smaller Q_S and larger Q_P as indicating larger shear attenuation than bulk attenuation.

[45] There are also some differences between our results and the results of *Schlotterbeck and Abers* [2001], which are likely caused by the difference in the size of the data sets used. For instance, they observed variability in Q of a factor of three whereas we find a variability factor of larger than 10. They reported an average Q_S/Q_P for the near surface of 1.5, while we obtain $Q_S/Q_P = 1.3$. They reported low Q values beneath the San Gabriel Mountains, which we did not detect. We interpret their San Gabriel anomaly to be smearing of low Q values associated with the adjacent basins, such as the east Ventura basin, into the mountain range.

[46] The variations in Q_P and Q_S with depth agree well with the findings of *Hough and Anderson* [1988]. In particular, they found very high Q layers interlaced with low Q layers at midcrustal depths. Our 3-D model exhibits similar features, with low Q zones interlaced at depth with zones of high Q. This Q structure in part explains the results of *Harmsen* [1997], who estimated diminution of amplitude in the frequency range from 0.5 to 8.0 Hz with distance in the greater Los Angeles area. His results showed that there was some suggestion that S waves from deeper sources decay faster.

[47] Our study as well as most previous studies of Q_P and Q_S in southern California have shown that $Q_S/Q_P > 1$. Using Anza data from the Peninsular Ranges, *Hough and Anderson* [1988] showed that $Q_S/Q_P > 1$. *Abercrombie* [1995] also found that on average, extending out to a distance of 120 km, $Q_S \sim 1.2\ Q_P$ using high-quality data from borehole seismometers in Cajon Pass, southern California. Her average $Q_P \sim 912$ and $Q_S \sim 1078$ are explained well by our model because the Cajon Pass borehole and the seismicity analyzed by *Abercrombie* [1995] are located within the high Q region of the northern Peninsular Ranges and the San Bernardino Mountains. *Lees and Lindley* [1994] also found $Q_S/Q_P > 1$ within the 1989 Loma Prieta aftershock zone. Similarly, *Prejean and Ellsworth* [2001] found $Q_S/Q_P > 1$ at seismogenic depths in the Long Valley Caldera, eastern California. They found $Q_P \sim 100$ and $Q_S \sim 200$ for earthquakes in the inner caldera to $Q_P \sim 400$ and $Q_S \sim 800$ for earthquakes south of the caldera. Further, *Yoshimoto et al.* [1998] showed that Q_S/Q_P values range from 1.3 to 2.9 in Nagano Prefecture in Japan and inferred that apparent attenuation for P and S waves is similar. If $Q_S/Q_P \sim 1$, the attenuation in shear and bulk modulus is of similar size [*Sarker and Abers*, 1998]. In our case with $Q_S/Q_P \sim 1.3$ the attenuation in shear is lower than the attenuation in bulk modulus. One possible interpretation of $Q_S/Q_P > 1$ is that both the P and S waves suffer similar intrinsic attenuation while the P waves suffer more from scattering.

4.4. Interpretation of 3-D Q Models and Velocity, Geology, and Seismicity

[48] Variations in Q_P and Q_S may be related to porosity, temperature variations, heterogeneity, grain boundary sliding, and lithology. If Q_P and Q_S are similar or drastically different in places, this may provide clues for the contribution of scattering, absorption, or temperature to Q. In southern California, we observe strong correlation with lithology, including large near-surface attenuation in sedimentary basins. Similarly, we observe a general correlation with the regional tectonics.

[49] The first-order feature of both the Q_P and Q_S models is the strong near-surface increase in attenuation. These prominent near-surface low Q_P and Q_S values were also detected by *Olsen et al.* [2003], who simulated 3-D wave propagation through the Los Angeles basin to determine the starting Q_P and Q_S models. They showed that attenuation has its largest effects on short-period surface waves propagating in the Los Angeles basin. These waves are most sensitive to low Q_S and low V_S near-surface sediments in the Los Angeles basin with the lowest Q_S values of ~10. We are not able to resolve such low Q values because the combination of sources and receivers available in this study do not sample the near surface (the uppermost few hundred meters) well enough. They also found that the ground motion simulations are relatively insensitive to Q_P.

[50] In general, the new 3-D Q and velocity models for southern California from *Hauksson* [2000] show similar results, although the features in the Q_P and Q_S models are usually broader and less sharp than the features in the 3-D velocity models. Both the Q values and the velocities increase with depth and exhibit similar large-scale spatial features such as slightly higher values to west of the San Andreas fault than to the east of the fault. The high Q values of the Peninsular Ranges extend across the San Andreas fault whereas the corresponding high velocities stop at the San Andreas. Thus the southern Mojave Desert, including the San Bernardino Mountains, are imaged with high Q values and only average velocity values, suggesting a difference in lithology or attenuation mechanisms between the Peninsular Ranges and the southern Mojave.

[51] As an example, the high Q_P and Q_S values within the Peninsular Ranges vary across the region and do not simply follow topography or gravity signatures. *Langenheim and Hauksson* [2001] predicted gravity from the 3-D V_P model of the upper crust and compared it to the observed isostatic residual gravity field. Both data sets showed similar variations in the upper crust, with a strong north-south anomaly cutting across the Peninsular Ranges. In contrast, the Q_P and Q_S variations exhibit a more complex spatial distribution with a clear correlation to velocity in the near surface, but the shapes of the Q_P and Q_S anomalies are broader and extend farther east than the V_P and gravity anomalies.

[52] Similar to applying traveltimes of body waves, surface wave dispersion can be used to map the near-surface velocity structure. Using a technique particularly sensitive

to surface velocities (V_S), *Shapiro et al.* [2005] used ambient seismic noise to invert for surface wave velocity. Near the surface, they showed that high velocities were found beneath the mountain ranges as opposed to the low velocities in the basins, thus their results are consistent with the near-surface Q values determined in this study.

[53] It is interesting to compare our Q_P and Q_S maps with heat flow maps (http://quake.usgs.gov/heatflow/). There is no simple correlation between heat flow and Q_P or Q_S. The high heat flow in the Salton Sea area corresponds well with low Q_P and Q_S, near the south shore of the Salton Sea. However, in the Peninsular Ranges, to the north and west of the Salton Sea, the high Q values correspond with the heat flow but the intermediate Q values to the northeast of the Salton Sea are inconsistent with similarly low heat flow. In particular, the high Q and low heat flow correlation breaks down in the Joshua Tree region where heat flow is very low but the Q is about average. Similarly, the low Q_P and Q_S values in the east Ventura basin are inconsistent with the low heat flow of the region. Thus other crustal properties appear to have a stronger influence on the Q than heat flow.

5. Conclusions

[54] We have determined 3-D Q_P and Q_S models of the southern California crust. These models have generally low Q_P and Q_S ($\sim$100) from 0 km down to 4 or 5 km depth, whereas the deeper layers have higher values of $Q_P \sim 500-900$ and $Q_S \sim 600-1000$, with a mean $Q_S/Q_P = 1.3$. The 3-D models also image regional variations in Q_P and Q_S that correlate with tectonic structures. Low Q_P and Q_S values exist in the sedimentary basins, such as the Santa Maria, eastern Ventura, Los Angeles, Chino, and San Bernardino basins and the Salton Trough. Similarly at shallow depth, the most obvious high Q_P and Q_S values are imaged within parts of the batholithic terrains such as the Peninsular Ranges, central Mojave, and southern Sierra Nevada. At midcrustal depths, interlacing of slightly lower Q values within zones of high Q suggest that such stacking may correspond to areas of high reflectivity, often observed in seismic reflection surveys. There is no obvious correlation with heat flow except for a small area within the Salton Trough, thus suggesting that other factors affect Q more strongly than heat flow. There are no sharp variations in Q_P or Q_S near the brittle-ductile transition, suggesting that the brittle-ductile transition may be a broad zone where the changes in shear or bulk rigidity are only gradual. The station residuals that correspond to the 3-D models are related to unknown station calibrations and minor features in the site geology that are not included in the 3-D model. In particular, the large positive station residuals correspond to stations located near the edges of sedimentary basins, possibly caused by multipathing or wave reverberations near the basin edge, which are difficult to account for in the smoothed 3-D models. The negative station residuals correspond to regions of very high Q in the near surface, which, due to the 15 km grid spacing and uneven ray coverage, may not be included in the final 3-D model. In general, $Q_S/Q_P > 1$, suggesting partially fluid-saturated crust for most of southern California. A few small regions of $Q_S/Q_P < 1$ suggest almost complete fluid saturation, which can explain large reductions in shear attenuation rather than in bulk attenuation.

Appendix A: Q_P and Q_S Model Quality

[55] The errors in the final 3-D Q models are caused by errors in the t^* determinations, inaccurate starting models, and errors related to the velocity models, such as incomplete parameterization and lack of resolution within certain parts of the model. We investigated sensitivity to the starting Q_P model, parameterization, and nonlinearity by trying different grids, different starting models, and different damping parameters. We have calculated the resolution matrix, the derivative weighted sum, and the standard error to evaluate effects of data errors, and uneven ray coverage.

[56] We calculate the model resolution matrix R for the damped least squares problem as [*Menke*, 1989]

$$R = \left(M^T M + L\right)^{-1} M^T M \tag{A1}$$

where M is the matrix of partial derivatives. If the resolution is perfect and the diagonal elements of the damping matrix L are all zero, the model resolution is the identity matrix. Using damping, we determine the values of the diagonal elements of the resolution matrix that range from 0 to 1.0, where 0 is unresolved and 1.0 is completely resolved. We did not save the full resolution matrix because it exceeds 1 Gbyte in size and does not add new information about the resolution of the model.

[57] The central parts of the Q_P and Q_S models are well resolved, whereas the edges and offshore areas to the west show low resolution (Figures A1 and A2). The spatial distribution of the Q_P and Q_S anomalies appears to be real because there are no obvious correlations between the poorly resolved regions and the anomalies in the final models (Figures 6 and 7).

[58] We calculated the model standard error to determine an estimate of the mapping of the data error into the model error. The standard error calculated from the covariance matrix is small and varies throughout the model with errors in Q_P and Q_S ranging from 0.01 to 0.5. Other studies using the same SIMULPS approach for velocity inversions have suggested that to obtain realistic standard error estimates the calculated standard error should be multiplied with a factor of 5. If we multiply with a factor of 5, the standard error remains small but would be similar to estimates in other studies such as by *Scherbaum* [1990]. He showed that the standard deviation of the final Q model ranged from 3% to 7%.

[59] The derivative weighted sum (DWS) of the nth Q parameter is defined as

$$\mathrm{DWS}(Q_n) = N \sum_i \sum_j \left\{ \int_{P_{ij}} \omega_n(x) ds \right\} \tag{A2}$$

where i and j are the indices for event and station, ω is the linear interpolation weight that depends on coordinate position, P_{ij} is the ray path from i to j, and N is the normalization for the volume influenced by Q_n [*Toomey and Foulger*, 1989].

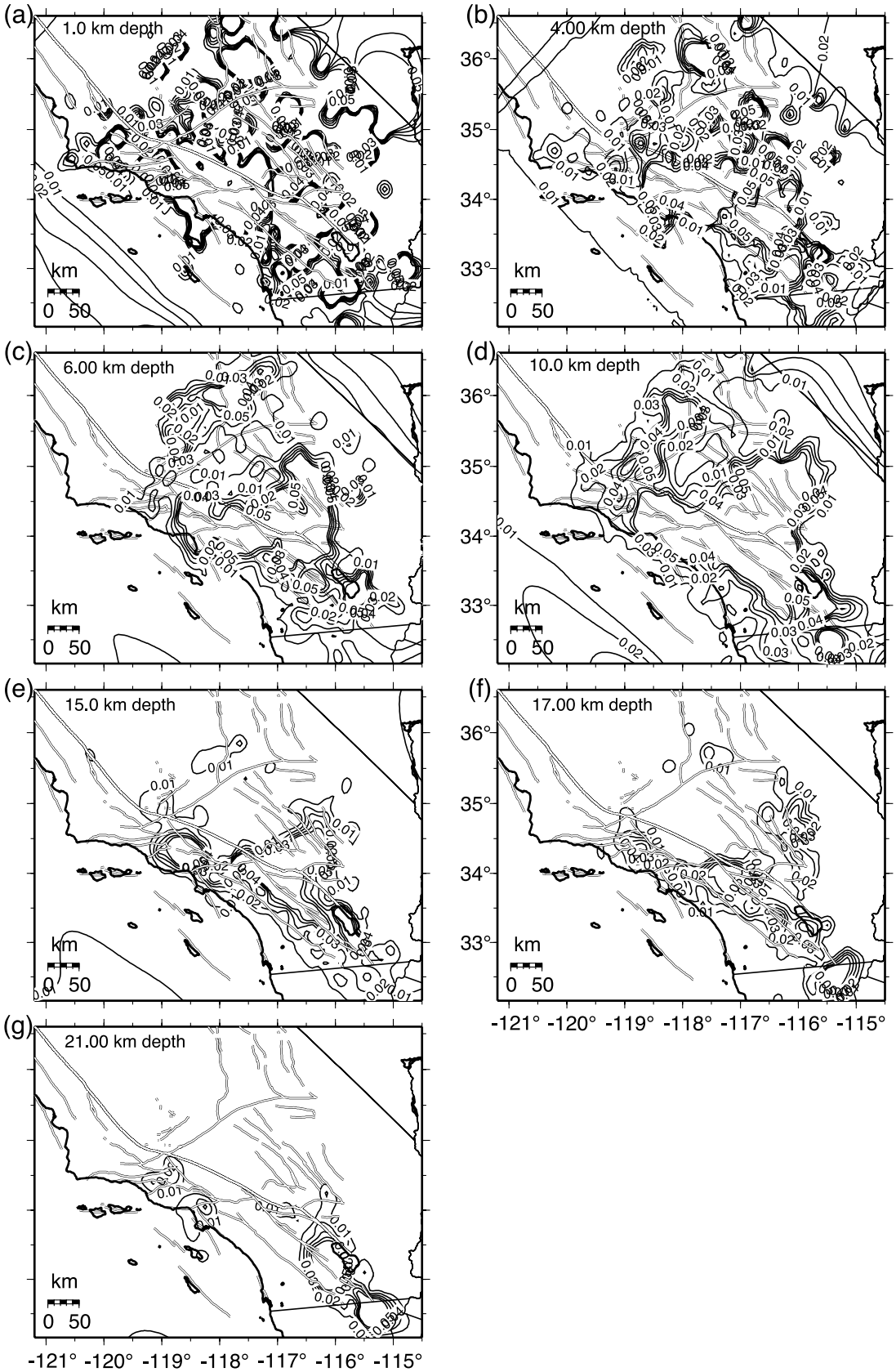

Figure A1. Diagonal elements of the resolution matrix for the final 3-D Q_P model shown in depth slices at 1, 4, 6, 10, 15, 17, and 22 km depth. The model is well resolved within the contour lines.

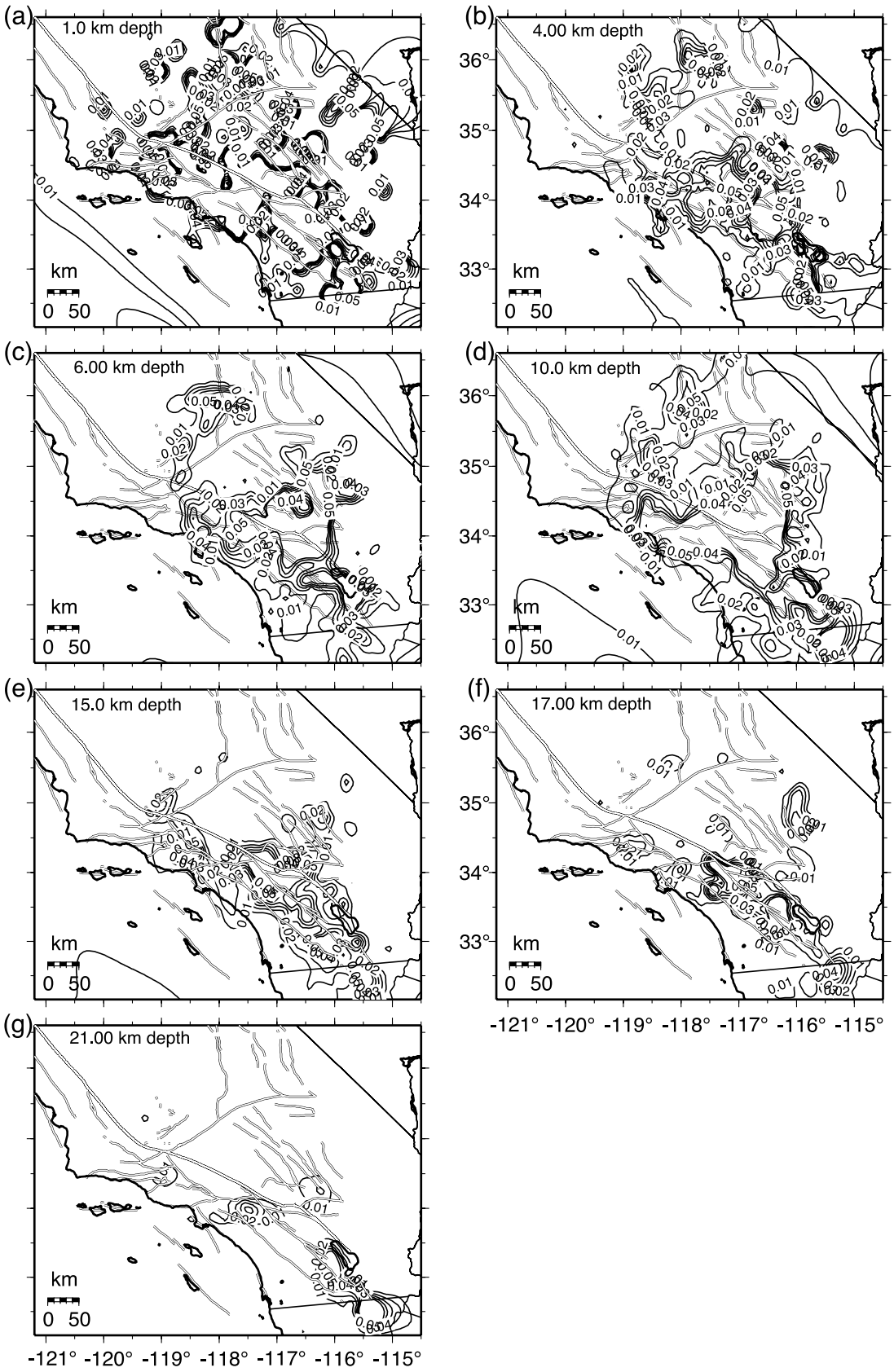

Figure A2. Diagonal elements of the resolution matrix for the final 3-D Q_S model.

[60] We use the DWS as a measure of the information density provided by the ray coverage. In general, the DWS values show that the 3-D Q_P and Q_S models are well resolved at depths from ~4 to 22 km. The near-surface layer and the bottom layers are poorly resolved (Figures 6 and 7).

[61] **Acknowledgments.** The Southern California Seismic Network (SCSN), Kate Hutton, and her staff, processed the data used in this study, and the data are archived at the Southern California Earthquake Data Center. We thank D. Eberhart-Phillips for making the *t** code available and C. Thurber for the SIMULPS code. We thank an anonymous and A. Rietbrock reviewers, the Associate Editor, H. Kanamori, J. Boatwright, and L. Jones for reviewing the manuscript. We also thank D. Eberhart-Phillips, H. Kanamori, S. Huusen, and J. Boatwright for stimulating discussions. The figures were done using GMT [*Wessel and Smith*, 1991]. Supported by NEHRP/USGS grants 04HQGR0052 and 05HQGR0040 and by SCEC, which is funded by NSF Cooperative Agreement EAR-0106924 and USGS Cooperative Agreement 02HQAG0008; SCEC contribution 953. Contribution 9127, Division of Geological and Planetary Sciences, California Institute of Technology, Pasadena.

References

Abercrombie, R. E. (1995), Earthquake source scaling relationships from −1 to 5 M_L using seismogram recorded at 2.5-km depth, *J. Geophys. Res.*, *100*, 24,015–24,036.

Abercrombie, R. E. (1997), Near surface wave attenuation and site effects from comparison of surface and deep borehole recordings, *Bull. Seismol. Soc. Am.*, *87*, 731–744.

Adams, D. A., and R. E. Abercrombie (1998), Seismic attenuation above 10 Hz in southern California from coda waves recorded in the Cajon Pass borehole, *J. Geophys. Res.*, *103*, 24,257–24,270.

Anderson, J. G., and S. E. Hough (1984), A model for the shape of the Fourier amplitude spectrum of acceleration at high frequencies, *Bull. Seismol. Soc. Am.*, *74*, 1969–1993.

Aster, R. C., and P. M. Shearer (1991), High-frequency borehole seismograms recorded in the San Jacinto fault zone, southern California, 2, Attenuation and site effects, *Bull. Seismol. Soc. Am.*, *81*, 1081–1100.

Atkinson, G. M., and R. F. Mereu (1992), The shape of ground motion attenuation curves in southeastern Canada, *Bull. Seismol. Soc. Am.*, *82*, 2014–2031.

Blakeslee, S. N., and P. E. Malin (1990), A comparison of earthquake coda waves at surface versus subsurface seismometers, *J. Geophys. Res.*, *95*, 309–325.

Brune, J. N. (1970), Tectonic stress and spectra of seismic shear waves from earthquakes, *J. Geophys. Res.*, *75*, 4997–5009.

Crowell, J. C. (1987), Late Cenozoic basins of onshore southern California: Complexity is the hallmark of their tectonic history, in *Cenozoic Basin Development of Coastal California*, vol. 6, edited by R. V. Ingersoll and W. G. Ernst, pp. 207–241, CRC Press, Boca Raton, Fla.

Eberhart-Phillips, D. (1986), Three-dimensional velocity structure in Northern California Coast Ranges from inversion of local earthquake arrival times, *Bull. Seismol. Soc. Am.*, *76*, 1025–1052.

Eberhart-Phillips, D. (1993), Local earthquake tomography: Earthquake source regions, in *Seismic Tomography: Theory and Practice*, edited by H. M. Iyer and K. Hirahara, pp. 613–643, CRC Press, Boca Raton, Fla.

Eberhart-Phillips, D., and M. Chadwick (2002), Three-dimensional attenuation model of the shallow Hikurangi subduction zone in the Raukumara Peninsula, New Zealand, *J. Geophys. Res.*, *107*(B2), 2033, doi:10.1029/2000JB000046.

Eberhart-Phillips, D., and G. McVerry (2003), Estimating slab earthquake spectra from a 3D Q model, *Bull. Seismol. Soc. Am.*, *93*, 2649–2663.

Erickson, Dirk, D. E. McNamara, and H. M. Benz (2004), Frequency-dependent *Lg Q* within the continental United States, *Bull. Seismol. Soc. Am.*, *94*, 1630–1643.

Frankel, A. (1991), Mechanisms of seismic attenuation in the crust: Scattering and anelasticity in New York state, South Africa, and southern California, *J. Geophys. Res.*, *96*, 6269–6289.

Frankel, A., A. McGarr, J. Bicknell, J. Mori, L. Seeber, and E. Cranswick (1990), Attenuation of high-frequency shear waves in the crust: Measurements from New York State, South Africa, and southern California, *J. Geophys. Res.*, *95*, 17,441–17,457.

Fuis, G. S., et al. (2003), Fault systems of the 1971 San Fernando and 1994 Northridge earthquakes, southern California: Relocated aftershocks and seismic images from LARSE II, *Geology*, *31*(2), 171–174.

Haberland, C., and A. Rietbrock (2001), Attenuation tomography in the western central Andes: A detailed insight into the structure of a magmatic arc, *J. Geophys. Res.*, *106*, 11,151–11,167.

Harmsen, S. C. (1997), Estimating the diminution of shear-wave amplitude with distance: Application to the Los Angeles, California, urban area, *Bull. Seismol. Soc. Am.*, *87*, 888–903.

Hauksson, E. (2000), Crustal structure and seismicity distributions adjacent to the Pacific and North America plate boundary in southern California, *J. Geophys. Res.*, *105*, 13,875–13,903.

Hauksson, E., and P. Shearer (2005), Southern California hypocenter relocation with waveform cross-correlation: part 1. Results using the double-difference method, *Bull. Seismol. Soc. Am.*, *95*, 896–903.

Hauksson, E., T. L. Teng, and T. L. Henyey (1987), Results from a 1500 m deep, three-level downhole seismometer array: Site response, low Q-values and f-max, *Bull. Seism. Soc. Am.*, *77*, 1883–1904.

Ho-Liu, P., H. Kanamori, and R. W. Clayton (1988), Applications of attenuation tomography to Imperial Valley and Coso-Indian Wells Region, southern California, *J. Geophys. Res.*, *93*, 10,501–10,520.

Hough, S. E., and J. G. Anderson (1988), High frequency spectra observed at Anza, California: Implications for *Q* structure, *Bull. Seismol. Soc. Am.*, *78*, 692–707.

Hough, S. E., L. Seeber, A. Lerner-Lam, J. C. Armbruster, and H. Guo (1991), Empirical Green's functions analysis of Loma Prieta aftershocks, *Bull. Seismol. Soc. Am.*, *81*, 1737–1753.

Jennings, C. W. (1994), Fault activity map of California and adjacent areas, scale 1:750,000, Calif. Div. of Mines and Geol., Sacramento.

Kanamori, H., J. Mori, E. Hauksson, T. Heaton, L. Hutton, and L. Jones (1993), Determination of earthquake energy release and M_L using TERRAscope, *Bull. Seismol. Soc. Am.*, *83*, 330–346.

Knopoff, L. (1971), Attenuation, in *Mantle and Core in Planetary Physics*, edited by J. Coulomb and M. Caputo, pp. 146–156, Elsevier, New York.

Langenheim, V., and E. Hauksson (2001), Comparison between crustal density and velocity variations in southern California, *Geophys. Res. Lett.*, *28*, 3087–3090.

Lees, J. M., and G. T. Lindley (1994), Three-dimensional attenuation tomography at Loma Prieta: Inversion of *t** for *Q*, *J. Geophys. Res.*, *99*, 6843–6864.

Lindley, G. T., and R. J. Archuleta (1992), Earthquake source parameters and the frequency dependence of attenuation at Coalinga, Mammoth lakes, and the Santa Cruz Mountains, California, *J. Geophys. Res.*, *97*, 14,137–14,154.

Menke, W. (1989), *Geophysical Data Analysis: Discrete Inverse Theory*, Univ. of Calif., San Diego.

Michelini, A., and T. V. McEvilly (1991), Seismological studies at Parkfield, I. Simultaneous inversion for velocity structure and hypocenters using cubic b-splines parameterization, *Bull. Seismol. Soc. Am.*, *81*, 524–552.

Nazareth, J. J., and E. Hauksson (2004), The seismogenic thickness of the southern California crust, *Bull. Seismol. Soc. Am.*, *94*, 940–960.

Olsen, K. B., S. M. Day, and C. R. Bradley (2003), Estimation of *Q* for long-period (>2 sec) waves in the Los Angeles basin, *Bull. Seismol. Soc. Am.*, *93*, 627–638.

Park, J., C. R. Lindberg, and F. L. Vernon (1987), Multitaper spectral analysis of high frequency seismograms, *J. Geophys. Res.*, *92*, 12,675–12,684.

Petukhin, A., K. Irikura, S. Ohmi, and T. Kagawa (2003), Estimation of *Q*-values in the seismogenic and aseismic layers in the Kinki region, Japan, by elimination of the geometrical spreading effect using ray approximation, *Bull. Seismol. Soc. Am.*, *93*, 1498–1515.

Prejean, S. G., and W. L. Ellsworth (2001), Observations of earthquake source parameters at 2 km depth in the Long Valley Caldera, eastern California, *Bull. Seismol. Soc. Am.*, *91*, 165–177.

Raoof, M., R. B. Hermann, and L. Malagnini (1999), Attenuation and excitation of three-component ground motion in southern California, *Bull. Seismol. Soc. Am.*, *89*, 888–902.

Rietbrock, A. (1996), Development of an interactive analysis for large seismological data sets: Application to the determination of the absorption structure in the Loma Prieta region, California, Ph.D. thesis, Ludwig-Maximulians-Univ. Munchen, Munich.

Rietbrock, A. (2001), *P* wave attenuation structure in the fault area of the 1995 Kobe earthquake, *J. Geophys. Res.*, *106*, 4141–4154.

Sarker, G., and G. A. Abers (1998), Deep structures along the boundary of a collisional belt: Attenuation tomography of *P* and *S* waves in the Greater Caucasus, *Geophys. J. Int.*, *133*, 326–340.

Sarker, G., and G. A. Abers (1999), Lithospheric temperature estimates from seismic attenuation across range fronts in southern and central Eurasia, *Geology*, *27*, 427–430.

Savage, J. C. (1974), Relation between *P*- and *S*-wave corner frequency in the seismic spectrum, *Bull. Seismol. Soc. Am.*, *64*, 1621–1627.

Scherbaum, F. (1990), Combined inversion for the three-dimensional Q structure and source parameters using microearthquake spectra, *J. Geophys. Res.*, *95*, 12,423–12,438.

Schlotterbeck, B. A., and G. A. Abers (2001), Three-dimensional attenuation variations in southern California, *J. Geophys. Res.*, *106*, 30,719–30,735.

Shapiro, N. M., M. Campillo, L. Stehly, and M. Ritzwoller (2005), High-resolution surface-wave tomography from ambient seismic noise, *Science*, *307*, 1615–1618.

Shearer, P. M., G. Prieto, and E. Hauksson (2006), Comprehensive analysis of earthquake source spectra in southern California, *J. Geophys. Res.*, doi:10.1029/2005JB003979, in press.

Thurber, C. H. (1993), Local earthquake tomography: Velocities and V_P/V_S-theory, in *Seismic Tomography: Theory and Practice*, edited by H. M. Iyer and K. Hirahara, pp. 563–583, CRC Press, Boca Raton, Fla.

Thurber, C., and D. Eberhart-Phillips (1999), Local earthquake tomography with flexible gridding, *Comput. Geosci.*, *25*, 809–818.

Toksoz, M. N., D. H. Johnston, and A. Timur (1979), Attenuation of seismic waves in dry and saturated rocks: I. Laboratory measurements, *Geophysics*, *44*, 681–690.

Toomey, D. R., and G. R. Foulger (1989), Tomographic inversion of local earthquake data from the Hengill-Grensdalur central volcano complex, Iceland, *J. Geophys. Res.*, *94*, 17,497–17,510.

Wessel, P., and W. H. F. Smith (1991), Free software helps map and display data, *Eos Trans. AGU*, *72*, 441, 445–446.

Yoshimoto, K., H. Sato, Y. Iio, H. Ito, T. Ohminato, and M. Ohtake (1998), Frequency-dependent attenuation of high-frequency P and S waves in the upper crust in western Nagano, Japan, *Pure Appl. Geophys.*, *153*, 489–502.

E. Hauksson, Seismological Laboratory, MS 252-21, California Institute of Technology, 1200 E. California Blvd., Pasadena, CA 91125, USA. (hauksson@gps.caltech.edu)

P. M. Shearer, Institute of Geophysics and Planetary Physics, Scripps Institution of Oceanography, University of California, San Diego, La Jolla, CA 92093-0225, USA. (pshearer@ucsd.edu)